

JGR Solid Earth

RESEARCH ARTICLE

10.1029/2020JB020799

Orogen-Parallel Migration of Exhumation in the Eastern Aar Massif Revealed by Low-T Thermochronometry



Key Points:

- Inversion of thermochronometry data reveals significant diachrony in the timing of exhumation along the strike of the Aar Massif
- Timing and pattern of exhumation are in good agreement with independent kinematic and age constraints from exposed shear zones
- Neogene exhumation was mainly controlled by thick-skinned compressional tectonics and efficient erosion of overlying sedimentary units

Supporting Information:

Supporting Information may be found in the online version of this article.

Correspondence to:

L. Nibourel,
lukas.nibourel@erdw.ethz.ch

Citation:

Nibourel, L., Rahn, M., Dunkl, I., Berger, A., Herman, F., Diehl, T., et al. (2021). Orogen-parallel migration of exhumation in the eastern Aar Massif revealed by low-T thermochronometry. *Journal of Geophysical Research: Solid Earth*, 126, e2020JB020799. <https://doi.org/10.1029/2020JB020799>

Received 17 AUG 2020

Accepted 27 SEP 2021

L. Nibourel^{1,6} , M. Rahn², I. Dunkl³ , A. Berger¹ , F. Herman⁴ , T. Diehl⁵ , S. Heuberger⁶ , and M. Herwegh¹ 

¹Institute of Geological Sciences, University of Bern, Bern, Switzerland, ²Institute of Earth and Environmental Sciences, University of Freiburg, Freiburg, Germany, ³Geoscience Center, University of Göttingen, Göttingen, Germany, ⁴Institute of Earth Sciences, University of Lausanne, Lausanne, Switzerland, ⁵Swiss Seismological Service, ETH Zurich, Zürich, Switzerland, ⁶Department of Earth Sciences, ETH Zurich, Zürich, Switzerland

Abstract New and published (U-Th)/He data on zircon, apatite, and zircon fission track ages constrain the thermal overprint and cooling history of the eastern Aar Massif, Switzerland. The timing and pattern of cooling is in agreement with independent kinematic and age constraints from exposed shear zones. This suggests that the cooling ages mainly reflect exhumation and that long-term exhumation-dynamics were mainly controlled by crustal-scale tectonic processes. Results of a statistical inverse model reveal significant diachrony in the timing of exhumation in the along-strike direction. Maximum exhumation rates (>1 mm/yr) were initially located in the central Aar Massif (from ~22 to 10 Ma), then gradually migrated to the east between ~10 Ma and present, while the central Aar Massif continued to exhume at slower rates (~0.5 mm/yr). The diachrony in the timing of exhumation may be explained by lateral variations in the inherited thickness or the density of the accreted European crust. We attribute the increase in exhumation rates between 2 Ma and present to enhanced glacial erosion. Nevertheless, the post 2 Ma exhumation pattern reflects a continuation of noncylindrical massif “growth” in the eastward orogen-parallel direction. This indicates that—although at slow rates—thick-skinned and buoyancy-driven compressional deformation, likely enhanced by the presence of easily erodible flysch units at the surface, might still be ongoing especially in the eastern Aar Massif. Noncylindrical massif-growth is likely to also affect other External Crystalline Massifs or orogens, but may be overlooked because studies often focus on single orogen-perpendicular transects.

Plain Language Summary The high topography of the Aar Massif in Switzerland formed in response to the collision of the European and the Adriatic tectonic plates and the associated thickening of the underthrust European crust. Erosion of this topography has exhumed deeply buried rock material which cooled as it approached the surface. We analyze new and published data, which document the timing and rate at which these rocks cooled on the way to the surface. Using a statistical model, we reconstruct how compressional crustal thickening, buoyancy forces and erosion interacted to form the Aar Massif. We find large variations in the timing and rate of exhumation, especially along the west-east axis of the massif. This is surprising given the south-north transport direction of the involved tectonic plates. When buried, a less dense crust will start to thicken and uplift earlier. Therefore, we attribute the early initiation of crustal thickening and rapid exhumation in the central Aar Massif to inherited irregularities in the thickness and density of the European crust. The shift of maximum exhumation rates from the central to the eastern Aar Massif appears to be enhanced by fast erosion of easily erodible sediments overlying less erodible crystalline basement of the Aar Massif.

1. Introduction

The exhumation of basement units from the thickened lower plate is a typical feature of advanced stages of collision in mountain belts such as the European Alps (e.g., Bellahsen et al., 2014; Herwegh et al., 2020; Rosenberg et al., 2018), the Pyrenees (e.g., Muñoz, 1992), or Taiwan (e.g., Simoes et al., 2007). This process is associated with thrusts or reverse faults, which drive uplift and erosion. The thereby exhumed basement blocks commonly form orogen-parallel structural domes with strong lateral variation.

© 2021 The Authors.

This is an open access article under the terms of the [Creative Commons Attribution-NonCommercial License](https://creativecommons.org/licenses/by-nc/4.0/), which permits use, distribution and reproduction in any medium, provided the original work is properly cited and is not used for commercial purposes.

Along the Western and Central European Alps, the External Crystalline Massifs (that is, from southwest to northeast, the Argentera, Pelvoux, Belledonne, Aiguilles Rouges, Mont Blanc, and Aar Massifs, Schmid et al., 2004, Figure 1a) represent examples of such lower plate basement exposures. These massifs form a laterally discontinuous belt of basement domes which are separated by structural saddles (e.g., Egli & Mancktelow, 2013).

In the past decades, many studies have used in situ thermochronometry to investigate the rapid Neogene cooling and exhumation of these massifs. Most of these studies have either focused on orogen-perpendicular transects (e.g., Boutoux et al., 2016; Glotzbach et al., 2010; Reinecker et al., 2008) or on lateral variations at the orogen scale (e.g., Fox et al., 2016; Vernon et al., 2008).

In the Aar Massif, the youngest published low-temperature thermochronometric ages (Glotzbach et al., 2010; Herwegh et al., 2020; Michalski & Soom, 1990; Rahn, 2001; Rahn et al., 1997; Reinecker et al., 2008; Valla et al., 2012; Vernon, van der Beek, Sinclair, Persano, et al., 2009) are not situated in the center of the dome, as would be expected from the structural relief and exposed metamorphic grade, but at its lateral edges, indicating complex along-strike exhumation dynamics (Figures 1 and 2).

Whether lateral variations in the cooling history and the massif's present geometry are controlled by the ongoing redistribution of mass through changes in the pattern of erosion and deposition, the spatial and temporal distribution of compression and extension within the crust or inherited structures remains difficult to answer, which is due to the strong coupling of these parameters (e.g., Fox et al., 2016; Robert et al., 2011; Sternai et al., 2019).

In this contribution, we investigate the role of tectonic processes during the Neogene exhumation of the eastern Aar Massif from maximum burial to the present, based on new and published (U-Th)/He data on zircon (ZHe), apatite fission track (AFT), and zircon fission track (ZFT) ages, together with published peak temperature data. A particularly high spatial resolution of thermochronometric and peak temperature constraints allows the timing and pattern of exhumation to be resolved in the orogen-perpendicular and orogen-parallel directions.

Many studies have investigated the Aar Massif (e.g., Herwegh et al., 2020), so that its tectonic architecture and evolution is well known. The European top basement, an orogen-scale marker, highlights the overall Alpine deformation and exhumation of the massif (Pfiffner, 2011, Figure 1). By assessing the geometric relationship between the present topography of the European top basement and cooling age patterns, we establish the timing of exhumation. A statistical inverse technique based on thermochronometric ages (Fox et al., 2014; Herman & Brandon, 2015) provides quantitative constraints on the space-time evolution of exhumation rates over the last ~16 Myr. Finally, we compare exhumation patterns to independent kinematic and age constraints from exposed shear zones to discuss the roles of tectonics, erosion, and structural inheritance during the formation and exhumation of the Aar Massif. Better understanding the fundamental controls of lateral variations in kinematics and exhumation rates at the scale of the Aar Massif (~100 km) and thus beyond major spatial variations in climate, may provide more general insight into the complex interaction of these parameters in other massifs or mountain belts.

2. Setting

2.1. Geological Architecture and Tectonic Evolution

The Aar Massif is a >120 km long and 20 km wide east-northeast-trending structural dome located in the Central Swiss Alps (Figure 1). It is classically viewed as the result of convergence between Europe and Adria and the associated post-35 Ma continent-continent collision (e.g., Froitzheim et al., 1996; Pfiffner, 2015; Schmid et al., 1996). The Aar Massif is the easternmost and largest External Crystalline Massif, exposing the crystalline basement of the thickened lower European plate (e.g., Schmid et al., 2004). The main tectonic units in the study area, in ascending tectonic position, are the Aar Massif basement including its sedimentary cover (Lower Helvetic), the Upper Helvetic and Penninic nappes (Figure 1). These units were generally emplaced in sequence from top to bottom and from south to north (Burkhard, 1988; Ramsay et al., 1983; Trümpy et al., 1980). The Helvetic nappes (Upper Helvetic) are interpreted to represent the sedimentary cover to the Gotthard and Tavetsch nappes, mostly consisting of crystalline basement (Figure 1, Trümpy

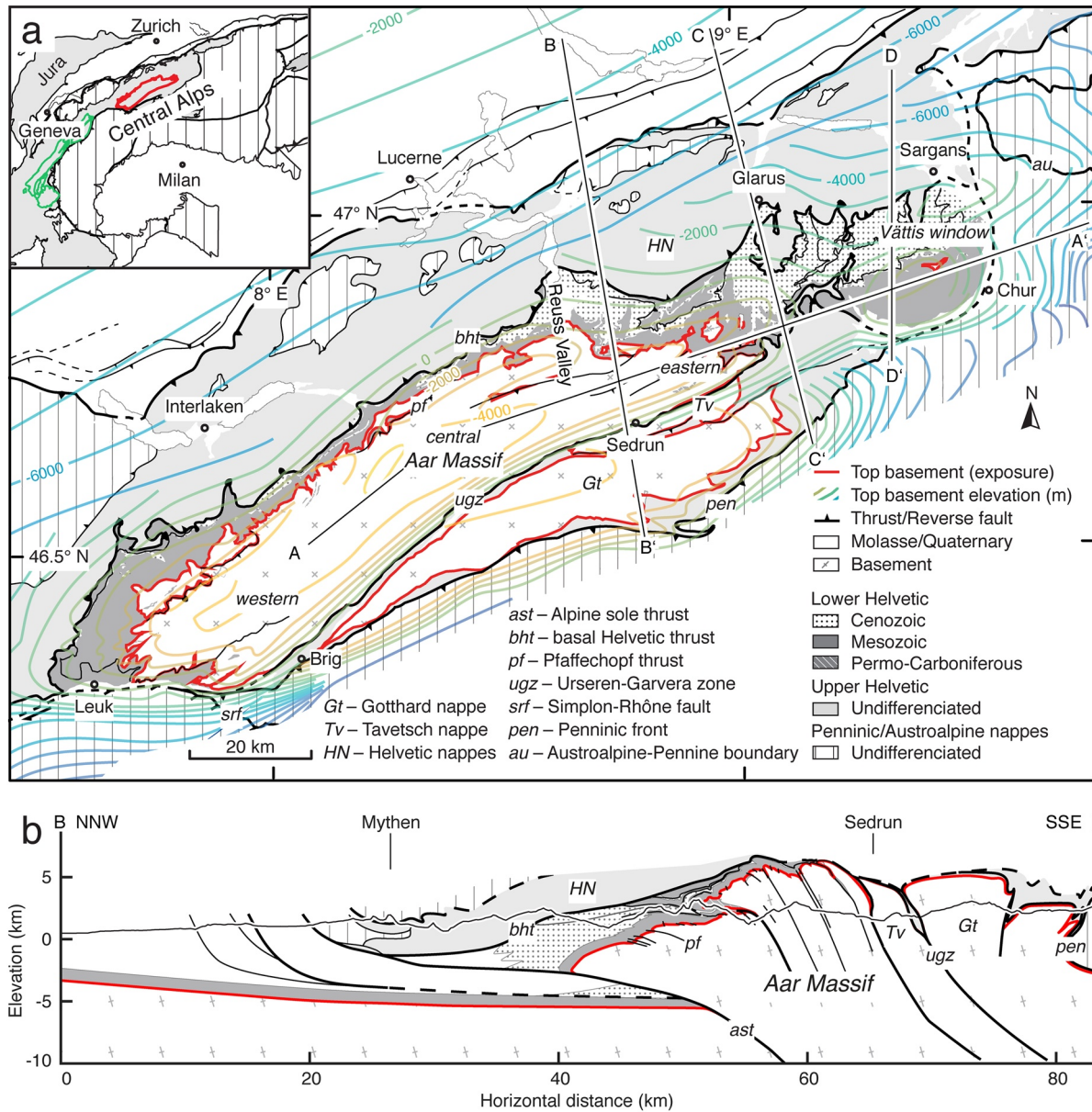


Figure 1. (a) Simplified structural map of the central Swiss Alps (modified from Schmid et al., 2004) and traces of cross sections A-A' (along-strike transect), B-B' (Reuss Valley transect), C-C' (Glarus transect), and D-D' (Vättis transect). Contour lines of the European top basement are adapted from Pfiffner (2011). The External Crystalline Massifs are highlighted in green (see inset). Profile edge coordinates for cross sections A-A', B-B', C-C', and D-D' are given in Text S1 in Supporting Information S1. (b) Cross section B-B' is after Brückner and Zbinden (1987), Pfiffner (2011), and Nibourel et al. (2021).

et al., 1980). They contain a carbonate shelf sequence with prominent massive limestones as well as sequences of marl and shale. In the east, Flysch and Bündnerschiefer units of the Penninic nappes, mostly consisting of marls and shales, are exposed (e.g., Schmid et al., 2004, Figure 1).

Deformation and exhumation of the Aar Massif has occurred relatively late and mostly postdates the emplacement of the overlying nappes as illustrated by passive folding and tilting of the basal Helvetic thrust (Figure 1b, Burkhard, 1988; Milnes & Pfiffner, 1977; Rahn & Grasemann, 1999; Schmid et al., 1996). The transition from the emplacement of the Helvetic nappes to basement-involved deformation in the Aar Massif coincides with a decrease in estimated convergence rates between Europe and Adria from ~13 mm/yr in the Oligocene to ~2 mm/yr in the Neogene (Handy et al., 2010; Schmid et al., 1996).

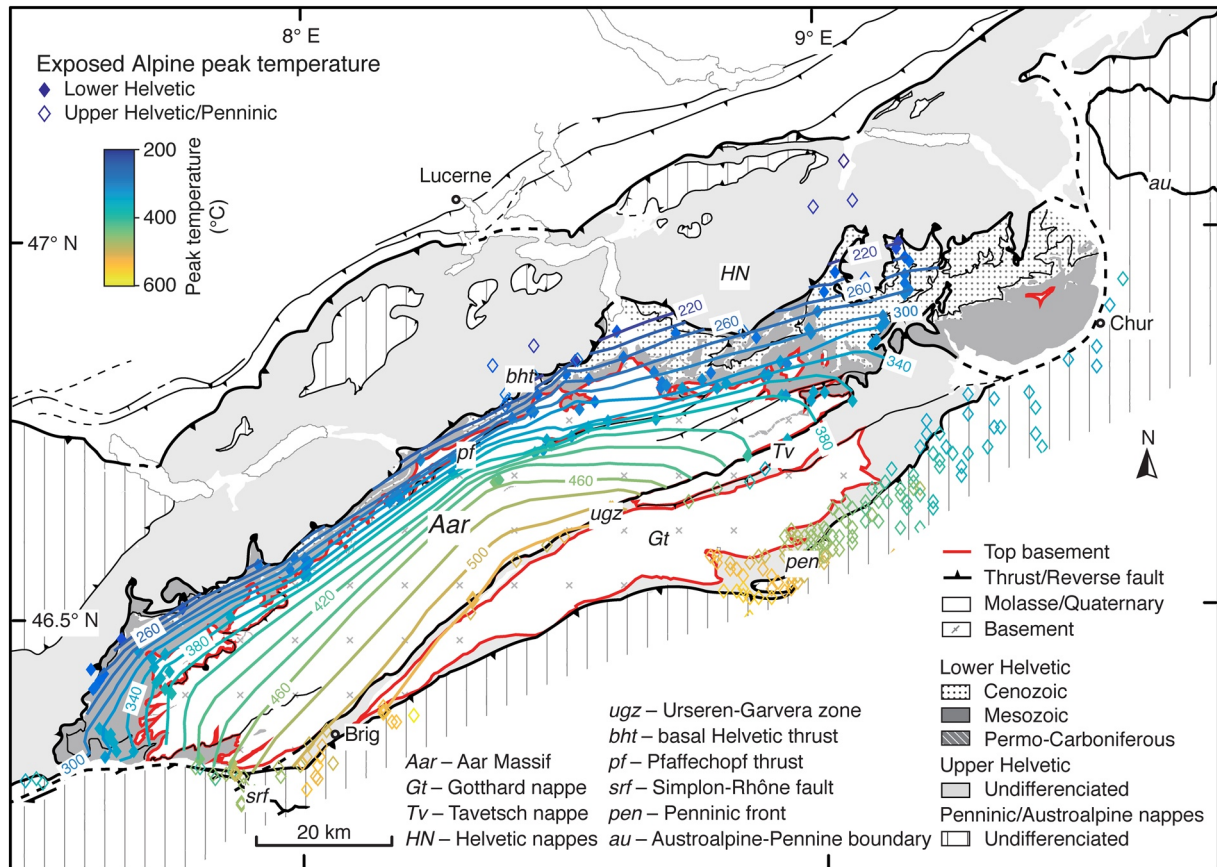


Figure 2. Simplified structural map modified from Schmid et al. (2004) including published peak temperature data based on Raman Spectroscopy on carbonaceous material (Berger et al., 2020; Beyssac et al., 2002; Erne, 2014; Girault et al., 2020; Hafner, 2016; Lahfid et al., 2010; Mair et al., 2018; Negro et al., 2013; Nibourel et al., 2018, 2021; Wiederkehr et al., 2011) and calcite-dolomite thermometry (Herwegh & Pfiffner, 2005). Isograd lines representing peak Alpine metamorphic temperature in the Lower Helvetic domain are from Nibourel et al. (2021).

The Aar Massif entered the Alpine orogenic wedge after ~34–28 Ma, as constrained by the Rupelian age of the youngest sediments deposited onto the Lower Helvetic domain prior to its burial below the Helvetic nappes (e.g., Lu et al., 2018; Menkveld-Gfeller et al., 2016). Massif-wide cooling and exhumation is recorded from ca. 20 Ma onwards (e.g., Fox et al., 2016; Herwegh et al., 2020).

The Aar Massif exposes a dense network of Alpine fault zones. The kinematics and the age of these fault zones have been investigated over the past decades, especially in the central Aar Massif (see Herwegh et al., 2017, 2020, for review). This gives us the opportunity (a) to independently constrain the timing of deformation and exhumation and (b) to assess the relationship between tectonics and exhumation. In the central Aar Massif, an early set of ductile steep to sub-vertical NW-SE striking shear zones with mostly S-block up kinematics was recognized (e.g., Choukroune & Gapais, 1983; Herwegh et al., 2017, in press; Nibourel et al., 2021; Steck, 1968; Wehrens et al., 2017, see Figure 1). These reverse faults were dated at ca. 21–17 Ma based on isotopic ages on syn-kinematic micas (Challandes et al., 2008; Rolland et al., 2009).

In the southern central Aar Massif, these reverse faults are overprinted by mostly east-west striking dextral strike-slip faults (Wehrens et al., 2017). The transition from compressional to transpressional tectonics occurred at 14–10 Ma, as indicated by isotopic ages on syn- to post-kinematic minerals from cross-cutting strike-slip faults and associated Alpine clefts (Bergemann et al., 2017; Berger, Wehrens, et al., 2017; Challandes et al., 2008; Janots et al., 2012; Ricchi et al., 2019; Rolland et al., 2009).

At the northern central massif front, the steep reverse faults are overprinted by an array of NNW-vergent thrusts (i.e., Pfaffeochopf thrusts, Figure 1, Mock, 2014; Nibourel et al., 2021; Wehrens et al., 2017). A

distinct jump of ZFT ages across the Pfaffenhopf thrust indicates active thrusting after ca. 13 Ma (Herwegh et al., 2020).

In the absence of larger basement exposures east of the Glarus area, structural investigations have mainly focused on the Lower Helvetic sediments (Käch, 1972; Milnes & Pfiffner, 1977; Pfiffner, 1972, 1978; Schmid, 1975). According to these authors, a penetrative greenschist facies foliation and associated shear zones dominate the structural appearance. For details on phases and overprinting relationships in the Glarus area, the reader is referred to Milnes and Pfiffner (1977), Gasser and Den Brok (2008), Herwegh et al. (2008), Dielforder et al. (2016), Dielforder (2017), and von Däniken and Frehner (2017). Both, foliation and associated faults are dipping to the south-southeast and are dominated by down-dip stretching lineations with mostly reverse kinematics.

In the adjacent Subalpine Molasse, compressional deformation initiated in the Oligocene (Kempf et al., 1999; Schlunegger et al., 1997) and lasted until ca. 6–4 Ma (Mock et al., 2020; von Hagke et al., 2012, 2014). In the Jura fold-and-thrust belt, the main phase of compressional deformation occurred from ca. 14 to 4 Ma (Becker, 2000; Looser et al., 2021). From ca. 5 Ma onwards, it is suggested that the entire North Alpine Foreland was affected by accelerated uplift and erosion (Cederbom et al., 2011; Schlunegger & Mosar, 2011; von Hagke et al., 2012). Despite decreasing convergence between Europe and Adria, fast and episodic exhumation focused on the Aar and other External Crystalline Massifs through the Neogene (e.g., Fox et al., 2016; Fügenschuh & Schmid, 2003; Vernon et al., 2008).

Two maxima of modern surface uplift rates coincide with the east and west corners of the exposed Aar Massif, while rates generally decrease toward the massif center (Schlatter, 2014). Geodetically derived modern uplift rates are generally consistent with estimated erosion rates from cosmogenic nuclides in river sediments (0.9 ± 0.3 mm/yr) over the past 0.4 to 1.5 ka (Wittmann et al., 2007). Geodetic analyses indicate ongoing north-south convergence in the central Alps at rates (<1 mm/yr) in the central Aar Massif, increasing to up to 2 mm/yr in the Eastern Alps (e.g., Sternai et al., 2019).

2.2. Age and Grade of Alpine Metamorphism

In order to quantify the amount and pattern of early cooling and relate it to exhumation, we analyze peak temperature estimates and associated independent age constraints. In this section, we first discuss the age of metamorphism and then present a compilation of peak temperature estimates for the study area (e.g., Figure 2).

Alpine metamorphism in the Lower Helvetics results from tectonic burial below the accreted Upper Helvetic, Penninic, and Austroalpine nappes. In the study area, the age and grade of exposed metamorphism increase across the basal Helvetic thrust from the Lower into the Upper Helvetic (Frey & Ferreiro-Mählmann, 1999; Hunziker et al., 1986). To account for such variations in the thermal overprint, peak temperature data and thermochronometric ages from the tectonically higher Upper Helvetic, Penninic, and Austroalpine units are highlighted with different symbols through this study (Figures 3–5).

In the Lower Helvetic, the age of Alpine peak metamorphism is not completely resolved. Available isotopic ages on Alpine greenschist facies sheet silicates are often ambiguous and can be interpreted as crystallization or cooling ages (e.g., Challandes et al., 2008; Hunziker et al., 1992; Rolland et al., 2009). In the central southern Aar Massif, the age of peak metamorphism can be estimated at 22–17 Ma based on Ar-Ar, Rb-Sr, and K-Ar data on micas, which are part of peak metamorphic mineral assemblages (e.g., Berger, Wehrens, et al., 2017; Challandes et al., 2008; Rolland et al., 2009). This age is also supported by thermal models suggesting that at least 10 Myr are required to heat the Aar Massif basement to its estimated peak temperature of 450°C, if instantaneous burial is assumed (Challandes et al., 2008). In the adjacent Urseren-Garvera zone (Figure 1), peak metamorphism was dated at 21–17 Ma based on U-Th-Pb ages on allanite (Janots & Rubatto, 2014). In the northern and eastern Aar Massif, the age of peak metamorphism is poorly documented. In these areas, the onset of cooling is constrained by the northernmost possibly reset ZFT ages, ranging between 27 and 17 Ma (Michalski & Soom, 1990; Wangenheim, 2016) and by retrograde hydrothermal monazites from Alpine clefts which were dated at 17–6 Ma (Bergemann et al., 2017; Janots et al., 2012; Ricchi et al., 2019).

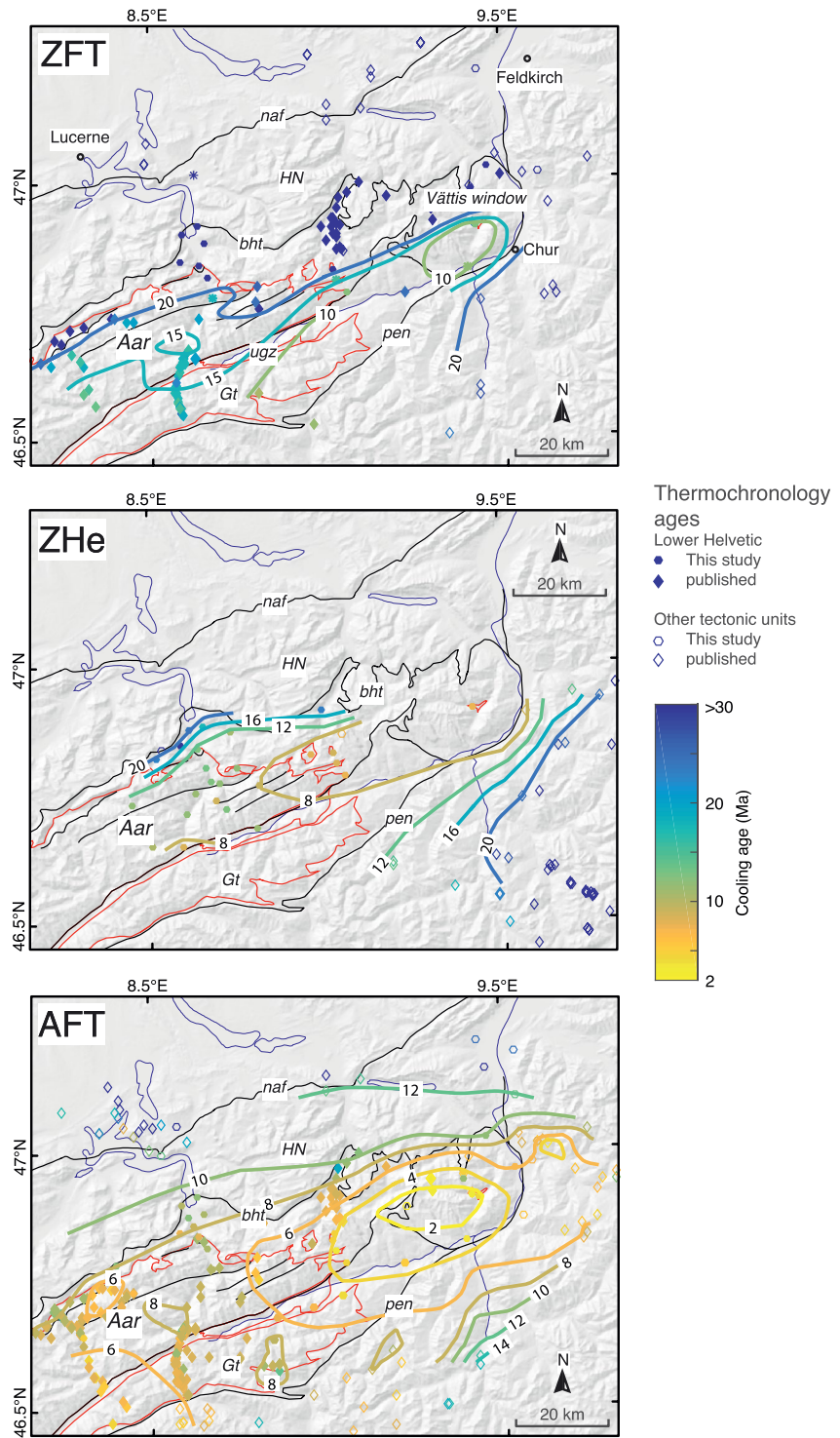


Figure 3. Spatial distribution of new and published zircon fission track (ZFT) and apatite fission track (AFT) central ages and unweighted mean (U-Th)/He ages on zircon (ZHe) including isoage contour lines for the 1,500 m elevation level. References are given in the text. All data are shown without filtering of unreliable or unreset ages. naf—Northern Alpine front, other abbreviations as on Figure 1.

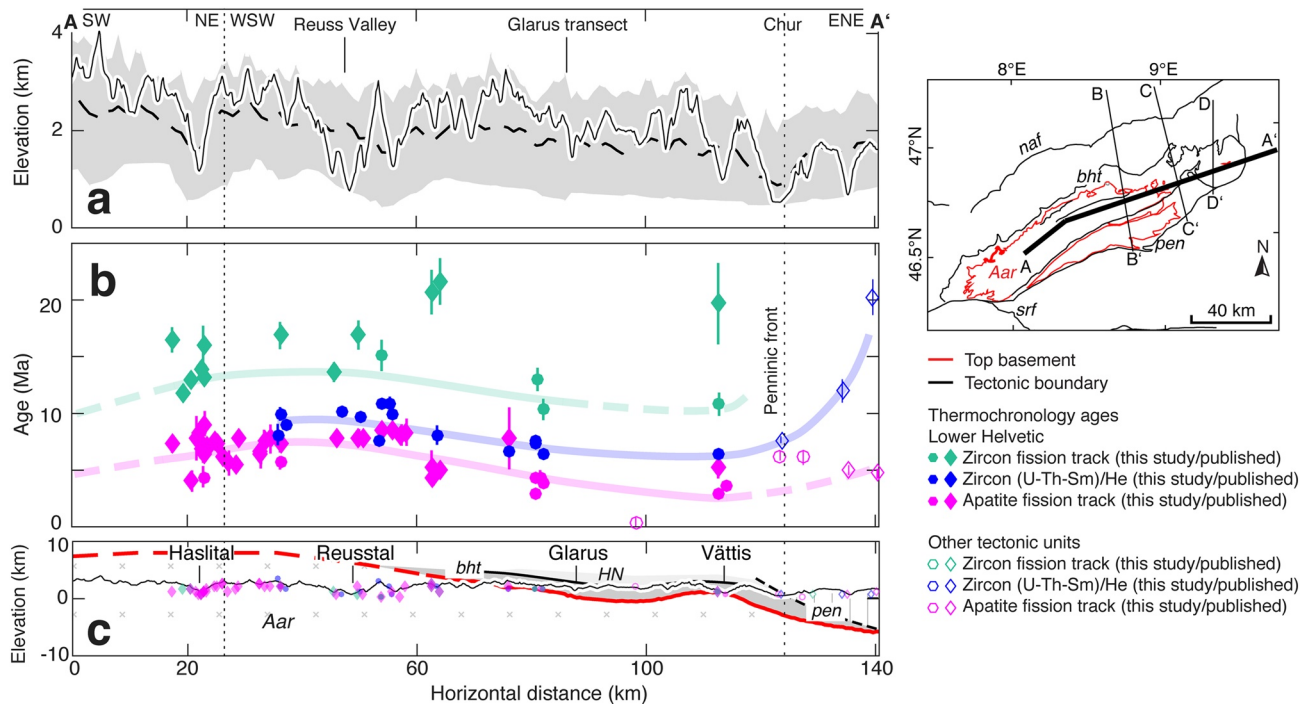


Figure 4. (a) Topography and topographic relief, (b) thermochronometric ages, and (c) structural relief along cross section A-A'. (a) Swath profile showing the present-day minimum and maximum elevation (gray, swath width = 20 km), mean elevation (dashed line), and topography along the section trace (thin black line). (b) New and compiled zircon fission track ages (ZFT), (U-Th)/He ages on zircon (ZHe), and apatite fission track ages (AFT) along the cross section (references are given in the text), normalized to 1,500 m. Age trends for ZFT, ZHe, and AFT data are qualitatively highlighted as bold lines. Maximum projection distance (perpendicular to section trace) = 5 km. (c) The cross section is partly based on Schmid (1975) and Pfiffner (2011). naf—Northern Alpine front, other abbreviations as on Figure 1. Additional information and profile edge coordinates are given in Texts S1 and S5 in Supporting Information S1. The asterisks and the thin dotted black lines indicate the northern front of the Aar Massif.

Alpine peak metamorphism in the Lower Helvetic reached sub-greenschist to greenschist facies conditions (Frey & Ferreiro-Mählmann, 1999). Figure 2 shows the exposed pattern of Alpine peak metamorphism in the lower Helvetic, based on published Raman thermometry and calcite-dolomite thermometry data (e.g., Nibourel et al., 2021). The peak-metamorphic grade generally increases from ~240°C in the north to 350–520°C in the south (i.e., Urseren-Garvera zone on Figure 2). Along strike, exposed peak temperature values decrease from up to 500°C in the center of the massif to 350°C toward its eastern rim, which reflects the easterly axial plunge of the eastern Aar Massif. In the following, we use the peak temperature pattern as a proxy for total exhumation between peak temperature conditions at ca. 22–17 Ma (in the central Aar Massif) and present.

2.3. Existing Thermochronometric Data

A number of thermochronological studies have been conducted in the Aar Massif and adjacent areas (references are given in the methods section). Reinecker et al. (2008) observed a two-fold increase of exhumation rates from ca. 0.5 to 1.2 mm/yr at 3.5 Ma and northward tilting of the western Aar Massif between 3.5 Ma and present. This was interpreted to reflect a change from orogen-parallel to orogen-perpendicular extension resulting in tectonic exhumation in the footwall of the Simplon-Rhône fault (Sue et al., 2007). In the central Aar Massif, thermochronometry studies revealed relatively steady exhumation at rates of 0.5 ± 0.2 mm/yr from ca. 12 Ma to present (Herwegh et al., 2020; Michalski & Soom, 1990; Vernon, van der Beek, & Sinclair, 2009; Vernon, van der Beek, Sinclair, Persano, et al., 2009), probably with pulses of accelerated exhumation occurring from 9 to 3 Ma (Vernon, van der Beek, Sinclair, Persano, et al., 2009). Wangenheim (2016) also found evidence for a post-2 Ma increase in relief due to enhanced glacial erosion, which is consistent with thermal modeling results from the southeast corner of the Aar Massif (Valla et al., 2012). For the Reuss Valley, Glotzbach et al. (2010) found nearly constant exhumation of ~0.5 mm/yr through the

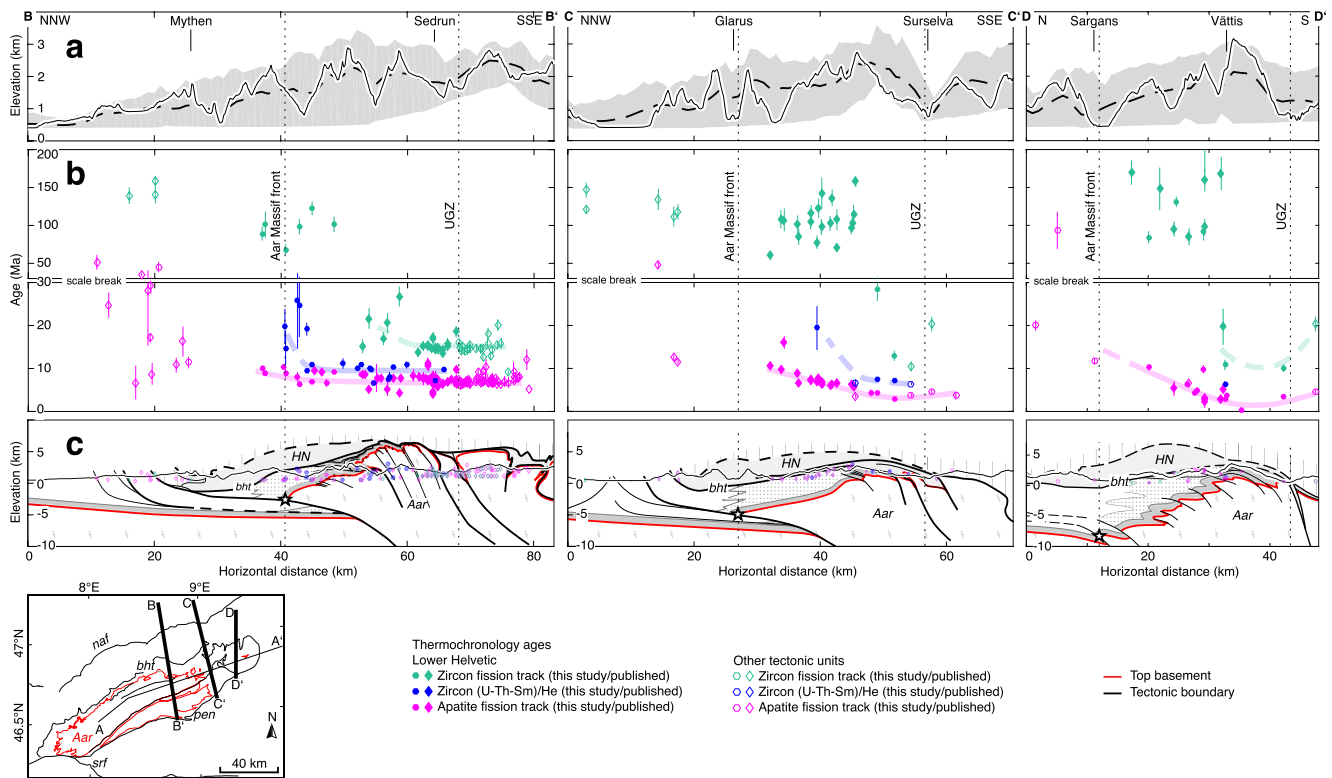


Figure 5. (a) Topography and topographic relief, (b) new and published zircon fission track ages (ZFT), (U-Th)/He ages on zircon (ZHe), and apatite fission track ages (AFT), and (c) major fault zones and top basement along cross section B-B' (left), C-C' (center), and D-D' (right). (a) The swath profile shows the present-day minimum and maximum elevation (gray, swath width = 20 km), mean elevation (dashed line) and topography along the section trace (thin black line). (b) Cooling ages along the cross section (references are given in the text), normalized to 1,500 m. Maximum projected distance perpendicular to the section trace = 15 km (cross sections B-B' and D-D'), 10 km (cross section C-C'). Age trends for ZFT, ZHe, and AFT data are qualitatively highlighted as bold lines. (c) Cross section B-B' is based on Nibourel et al. (2018). Cross sections C-C' and D-D' are simplified from Pfiffner (2011). Profile edge coordinates are given in Text S1 in Supporting Information S1. naf—Northern Alpine front, other abbreviations as on Figure 1.

past 14 Myr, but two possible phases of accelerated exhumation at 16 to 14 Ma and at 10 to 7 Ma. These authors interpreted the Aar Massif to be in long-term exhumational steady state and not affected by recent tectonic activity or climate change. In the Glarus area, Rahn et al. (1997) and Rahn and Grasemann (1999) found evidence for differential exhumation including the northward tilting of the northern parts of the basal Helvetic thrust plane by $\sim 7^\circ$ after the closure of the AFT system between 5 and 12 Ma, which they related to active shortening in the Aar Massif (Figure 1). At the east corner of the massif (Vättis area), Persaud and Pfiffner (2004) observed a spatial correlation between young AFT cooling ages, post-glacial reverse faulting, seismic activity and geodetically derived modern uplift rates, which they attributed to active compressional tectonics. Overall, a complex picture has emerged from these studies. The timing of exhumation appears to vary along the strike of the Aar Massif, but also at the scale of the orogen (e.g., Fox et al., 2016).

2.4. Detrital Thermochronometry and Sediment Budget Analysis

Detrital thermochronometry is commonly used to study variations in erosion rate, especially as averaged over large regions. Overall, the lag time of the youngest populations of zircons in Alpine sediments (i.e., difference between the depositional and the ZFT cooling age), indicate relatively steady peak exhumation rates of ~ 1 mm/yr at the scale of the orogen since ca. 30 Ma (Bernet & Spiegel, 2004; Bernet et al., 2001, 2004, 2009; Dunkl et al., 2001; Glotzbach, Bernet, & van der Beek, 2011; Spiegel et al., 2000). In contrast, sediment budget analysis reveals a more than two-fold increase of sediment yield since ~ 5 Ma (Kuhlemann, 2000; Kuhlemann & Kempf, 2002). This increase coincides with the transition to a more erosive climate and with the Messinian salinity crisis (Willett et al., 2006). Although there is significant uncertainty attached to the

estimation of sediment volumes in the Alpine foreland basins, these very contrasting observations have stimulated research on feedback mechanisms between tectonic and climatic processes (e.g., Willett, 2010).

3. Methods

3.1. New and Compiled Low-T Thermochronometry Data

Thermochronometry quantifies the timing and velocity at which rocks cool, for example, as they approach the earth's surface as a result of exhumation (e.g., Reiners & Brandon, 2006, see also Text S2 in Supporting Information S1). A thermochronometric cooling age records the time elapsed since a rock cooled through a given temperature, generally referred to as closure temperature (T_c , Dodson, 1973). If the closure temperature is at a known depth (closure depth), a thermochronometric age simply corresponds to the time required to move from that depth to the surface (Willett & Brandon, 2013) and can thus be used to infer exhumation rates. However, knowing the closure depth of a given thermochronometric age requires an understanding of the thermal structure of the crust and the cooling rate at the time equivalent to the cooling age (e.g., Reiners & Brandon, 2006). Besides exhumation, cooling ages can also be affected by processes such as hydrothermal activity, in situ heat production or thermal relaxation after peak metamorphism.

The fission track method is based on the retention of damage trails (fission tracks), which are induced by the spontaneous fission of ^{238}U contained in zircon or apatite (e.g., Reiners & Brandon, 2006, see also Text S3 in Supporting Information S1). Partial annealing of fission tracks usually occurs between 190°C and 380°C in zircons and between 60°C and 120°C in apatites (Rahn et al., 2004). Associated closure temperatures range from 190°C to 260°C for the ZFT system and from 80°C to 190°C for the AFT system (calculated for fluorapatite and radiation damaged zircon, using the program Closure, Brandon et al., 1998). The low and high values represent slow and fast cooling rates, respectively.

In apatite, the annealing capacity of fission tracks is strongly influenced by the ratio between Cl and F (e.g., Green et al., 1986). Fission tracks in fluorine-rich apatites anneal more rapidly than in chlorine-rich apatites (Crowley et al., 1991; Donelick et al., 1999; Green et al., 1986). This compositional influence is estimated by measuring Dpar values, reflecting the length of etch pits parallel to the crystallographic *c*-axis (Burtner et al., 1994). Partial annealing in fluorine-rich apatites (Dpar $\leq 1.75 \mu\text{m}$) occurs at temperatures of $110 \pm 20^\circ\text{C}$, while partial annealing in chlorine-rich apatites (Dpar $\geq 1.75 \mu\text{m}$) occurs at temperatures of $130 \pm 20^\circ\text{C}$ (Donelick et al., 2005).

The annealing kinetics of ZFTs particularly depend on radiation damage in the crystal (Garver et al., 2005; Kasuya & Naeser, 1988; Rahn et al., 2004). In zircons with little radiation damage, fission tracks anneal at temperatures between ~ 280 and 300°C (Garver et al., 2005). In contrast, fission tracks in radiation damaged zircons anneal at ~ 180 – 200°C (Garver et al., 2005).

The ZHe method is based on the radioactive decay of ^{238}U , ^{235}U , ^{232}Th , and ^{147}Sm isotopes and the associated retention of the daughter product ^4He in a zircon crystal below a given closure temperature (e.g., Reiners & Brandon, 2006, see also Text S4 in Supporting Information S1). He retention in zircon, among other factors, is mainly affected by the crystal size and morphology, anisotropy, source zonation, and on radiation damage (Farley et al., 1996). While the effects of crystal size, morphology and source zoning are routinely estimated by applying an alpha ejection correction (e.g., Hourigan et al., 2005), interactions between radiation damage and He diffusivity appear to be more complex (e.g., Guenther et al., 2013). The degree of radiation damage depends on the concentration of effective uranium (eU) and on the time elapsed since the sample has cooled below the partial annealing zone. Positive eU-age relationships appear to reflect isolated radiation damage zones interrupting existing crystallographic He diffusion pathways in crystals with relatively little radiation damage (Guenther et al., 2013). Negative eU-age relationships are considered to be the result of interconnected damage zones generating suitable pathways for He diffusion in zircons with moderate to high radiation damage (Guenther et al., 2013). The degree of radiation damage can be estimated with Raman Spectroscopy (Nasdala et al., 2004). The closure temperature of the ZHe system is estimated at 140°C – 195°C (Reiners et al., 2002; Stockli, 2005). In crystals with high alpha damage densities, it can be even lower (Guenther et al., 2013).

For AFT, ZFT, and ZHe analysis, apatite and zircon bearing lithologies were mostly collected from the Lower and Upper Helvetic (see Table S1 in Supporting Information S1 for sample information). Complementary to the intensively studied Lötschberg (western Aar Massif, Reinecker et al., 2008), Haslital (Vernon, van der Beek, Sinclair, Persano, et al., 2009; Wangenheim, 2016), Reuss Valley (Glotzbach et al., 2010), and Glarus (Rahn et al., 1997) transects, we provide 18 new ZFT, 29 new ZHe, and 47 new AFT ages for the central to eastern Aar Massif and adjacent regions (Figure 2). For AFT and ZFT analysis, 7–40 grains per sample were analyzed depending on the availability of grains and the central age was plotted for each sample. Two to four grains per sample were measured for ZHe analysis and the sample age represents an unweighted mean age. Single grain ZHe ages which were identified as outliers based on the Dixon and the Grubbs tests were rejected for the calculation of the unweighted average sample age (Table 1, Dixon, 1950; Grubbs, 1950, see also Tables S4–S6 in Supporting Information S1). For sample disaggregation and mineral separation, standard procedures were applied (selfrag, jaw crusher, mill, sieve shaker, Wilfley table, magnetic separator, heavy liquids, Hurford, 1990; Hurford & Green, 1982, see Text S4 in Supporting Information S1). AFT and ZFT analysis was conducted by M. Rahn, mostly at University of Basel, Switzerland. ZHe analysis was conducted at the Geoscience Centre, University of Göttingen in Germany.

In addition to the 94 new thermochronometric ages, we compiled 595 AFT, (U-Th)/He on apatite (AHe), ZFT, and ZHe ages from previous studies (Berger et al., 2020; Campani et al., 2010; Cederbom et al., 2004; Ciancaleoni, 2005; Elfert et al., 2013; Evans, 2011; Giger, 1991; Glotzbach et al., 2009; 2010; Hess, 2003; Hunziker et al., 1992; Hurford, 1986; Janots et al., 2008; Keller et al., 2005; Lihou et al., 1995; Michalski & Soom, 1990; Mock et al., 2020; Price et al., 2018; Rahn, 1994, 2001; Rahn et al., 1997; Reinecker et al., 2008; Schaer et al., 1975; Spiegel et al., 2000, 2001; Steiner, 1984; Timar-Geng et al., 2004; Valla et al., 2016; Vernon, van der Beek, Sinclair, Persano, et al., 2009; von Hagke et al., 2012, 2014; Wagner & Reimer, 1972; Wagner et al., 1977, 1979; Weh, 1998; Weisenberger et al., 2012), by building on an existing compilation by Fox et al. (2016). These are the data that are shown on Figures 3–5, with no filtering of potentially unreliable ages applied.

In contrast, only ages fulfilling the criteria given below were selected for inverse modeling (Table 1, Figures 6–8). ZFT and AFT ages which did not pass the χ^2 test at the 5% level were excluded as highlighted in Table 1 (see Tables S2 and S3 in Supporting Information S1, for details). Ages of poor quality (e.g., <10 grains analyzed for AFT/ZFT) and AHe/ZHe ages for which the standard deviation differs for more than 100% or 10 Ma from the average, or ages that were reported as such in the literature were rejected. Ages based on the population method were also excluded (for details, see Gallagher et al., 1998). Where age uncertainties have not been reported, a conservative value of 20% was assigned. Only ages <30 Ma were classified as likely Alpine reset. This age limit corresponds to the initiation of burial of the Lower Helvetic in the footwall to the basal Helvetic thrust, as indicated by the Rupelian age of the youngest sediments in the Lower Helvetic (Menkveld-Gfeller et al., 2016). Ages ≥ 30 Ma were not considered for the qualitative analysis of cooling age patterns and the inverse modeling.

Our study represents a regional update of the results presented in Fox et al. (2016) who studied the exhumation history at the orogen scale. We re-evaluate the exhumation history of the eastern Aar Massif by considering 171 new and recently published thermochronometric ages. Especially the 51 new and recently published (Price et al., 2018) ZHe ages significantly improve the spatial and temporal resolution in the study area.

3.2. Qualitative Analysis of Regional Cooling Age Patterns

The good spatial resolution allows cooling age patterns to be evaluated in map (Figure 3) and in section view (Figures 4 and 5). For this qualitative evaluation, we used all ages with no filtering. To highlight regional age trends rather than local age differences which may to a first order reflect the high variability in sample elevation ranging between 400 and 3,500 m (Table S1 in Supporting Information S1), we performed an elevation correction on the cooling ages. Age elevation relationships of 0.7 km/Myr (ZFT), 0.7 km/Myr (ZHe), and 0.5 km/Myr (AFT) were used for the correction and represent mean values for the Lower Helvetic of the study area. Comparable values were found by Rahn et al. (1997) and Glotzbach et al. (2010). The ages were corrected to the 1,500 m elevation level, which approximately corresponds to the mean topography and sample elevation in the study area.

Table 1

New Thermochronometric Zircon Fission Track (ZFT), Apatite Fission Track (AFT), and (U-Th)/He Ages on Zircon (ZHe)

Sample	Latitude	Longitude	Elevation (m)	Central ZFT age (Ma) ^a	1 σ (Ma)	Central AFT age (Ma) ^a	1 σ (Ma)	Unweighted ZHe mean age (Ma) ^a	1 σ (Ma)
KAW 2408	8.30331	46.64358	1,140			3.7 <i>e</i>	1.1		
KAW 2983	9.21767	46.78026	710			3.1 <i>e</i>	0.5		
MR P 025	8.57672	47.05338	590			43.3 <i>e</i>	6.9		
MR P 027	8.62301	47.01549	450	258.3	21.9				
MR P 032	8.63257	46.91338	600	88.3 <i>e</i>	8.9	8.2	0.5		
MR P 035	8.58290	46.84641	1,830	99.3 <i>e</i>	9.5	7.1	0.6	25.2	4.3
MR P 037	8.62032	46.85763	675			6.3 <i>e</i>	1.1		
MR P 039	8.63290	46.83951	480	120.9 <i>e</i>	8.6	4.9	0.4		
MR P 040	8.65013	46.88278	675	67.4 <i>e</i>	7.4	7.2	1.0	11.6	0.3
MR P 042	8.60853	46.87620	520			8.3	0.6		
MR P 043	8.58853	46.89799	560	99.9 <i>e</i>	16.7	6.9	0.6	11.7	3.2
MR P 046	9.41186	46.98250	2,050	132.2 <i>e</i>	6.6	7.4 <i>e</i>	0.6		
MR P 048	9.45373	47.02271	490	83.3 <i>e</i>	7.7	8.2	0.7		
MR P 049	9.58764	46.97556	530			4.2	0.8		
MR P 051	9.53785	46.96307	760			4.8	0.5		
MR P 054	9.60267	47.01253	2,370	149.2 <i>e</i>	15.4	8.7	0.6		
MR P 058	9.39141	46.95541	2,755			6.9	0.6		
MR P 060	9.39039	46.95245	2,580			7.0	0.8		
MR P 062	9.39148	46.94272	2,180	92.3 <i>e</i>	11.3	11.2	1.0		
MR P 065	9.43466	47.21038	620	149.3 <i>e</i>	13.4	18.7 <i>e</i>	1.6		
MR P 100	9.05145	46.78435	1,530	10.4 <i>e</i>	1.1	3.9	0.5	6.5	0.3
MR P 101	9.53982	47.18808	470			17.9	1.2		
MR P 140	9.45657	47.15754	750			91.8 <i>e</i>	24.5		
MR P 142	9.54431	47.10099	860			10.4	0.8		
MR P 144	9.43159	46.90828	1,000			2.7	0.4		
MR P 146	9.39610	46.82440	600	8.7	0.9	1.6	0.2		
MR P 148	9.02587	46.80513	1,880	13.6	1.2	3.6	0.3	7.8	0.3
MR P 149	9.55882	46.86829	820			3.6	0.7		
MR P 151	9.01899	46.83870	1,870			5.1	0.8		
MR P 153	8.65852	46.81315	485	100.1 <i>e</i>	9.8	7.2	0.5		
MR P 154	8.67115	46.77505	510	13.7	1.6	6.7	0.5	9.4	0.2
MR P 155	8.52992	46.99797	530			9.4 <i>e</i>	1.4		
MR P 167	9.01574	46.82839	1,845	28.9 <i>e</i>	2.7	5 <i>e</i>	0.4	8.0	0.2
MR P 169	9.41513	46.91055	1,205	10.4 <i>e</i>	1.2	2.4 <i>e</i>	0.3	6.0	0.6
MR P 175	8.18432	46.71926	610			9.2 <i>e</i>	0.7		
MR P 211	9.22471	46.88983	2,360			2.0 <i>e</i>	0.7		
MR P 215	8.79791	46.58837	1,915			7.5	1.2		
MR P 216	8.84397	46.63333	1,490			8.4	1.5		
MR P 217	8.85588	46.67907	1,230			5.8	1.1		
MR P 218	8.95567	46.69704	1,245			5.6	1.1		
MR P 219	9.04306	46.71798	2,155			5.0	1.0		

Table 1
Continued

Sample	Latitude	Longitude	Elevation (m)	Central ZFT age (Ma) ^a	1 σ (Ma)	Central AFT age (Ma) ^a	1 σ (Ma)	Unweighted ZHe mean age (Ma) ^a	1 σ (Ma)
MR P 260	9.31517	46.65768	2,110			5.3	0.8		
MR P 283	8.44624	46.72895	2,225			7.1	0.7	11.0	0.7
MR P 284	8.40170	46.78430	1,905			11.3 <i>e</i>	2.0		
MR P 297	8.81967	46.86269	1,360			6.4 <i>e</i>	0.9		
MR P 299	8.24843	46.86006	670			8.2	1.0		
MR P 303	8.10985	46.65244	1,950			10.4 <i>e</i>	1.1		
MR P 466	8.45512	46.69893	3,502			9.7	0.7		
MR T 009	9.04482	46.86470	3,100					8.9	0.9
MR T 180	8.98439	46.91187	875					18.5	5.1
EZ-15-07	8.71413	46.71901	2,200					11.8	0.8
BR-15-05	8.80540	46.76570	2,060					8.9	1.0
ME-15-03	8.60251	46.71170	990					9.5	0.3
GO-15-01	8.50146	46.65014	1,760					9.4	0.3
AN-15-01	8.59034	46.64650	1,420					7.1	0.1
GU-15-01	8.62770	46.75094	1,250					9.3	0.4
TO-15-04	8.95433	46.82365	1,850					7.2	0.3
KL-15-06	8.72560	46.86983	850					23.3	7.7
AL-15-01	8.61138	46.87460	450					18.3	4.1
ER-15-30	8.63253	46.83921	480					9.4	0.4
ER-15-31	8.65796	46.79964	550					9.8	1.2
MA-15-03	8.69494	46.76889	770					8.9	0.2
TV-15-01	8.79949	46.68341	1,560					9.9	0.6
ME-15-04	8.45510	46.69882	3,500					11.0	1.1
WI-16-04	8.74390	46.79872	2,300					19.5	1.5
SU-16-01	8.53172	46.83688	2,390					26.1	9.3
SU-16-04	8.51315	46.81879	1,750					11.2	0.3
BR-16-02	8.68145	46.73716	3,070					9.8	0.3

^a*e* = excluded for inverse modeling.

Such a global elevation correction may introduce minor artifacts, especially in regions with spatial variations in the cooling history. However, major artifacts can be excluded as they would have been recognized during the careful inspection of the isoage patterns in section view. The elevation correction was not applied for the quantitative assessment described in the following chapter. It only serves to give the reader a fast overview of the spatial distribution of the ages. For this purpose, the simple global correction applied appears to be adequate.

The isoage contour lines shown in Figure 3 were calculated using the marching squares interpolation method provided in Matlab R2015B with a 2×2 km grid size. The isoage contour lines were then manually adjusted in the vicinity of anomalous ages (less than 15 ages) and masked in areas with poor data coverage. Most of these ages were possibly affected by local fluid flow and have been identified as such in the original publications. Adjustments were made with great care to ensure that isoage contour lines highlight the regional age trends. No potentially arbitrary constraints such as tectonic boundaries were used in this initial interpolation or the subsequent minor adjustments.

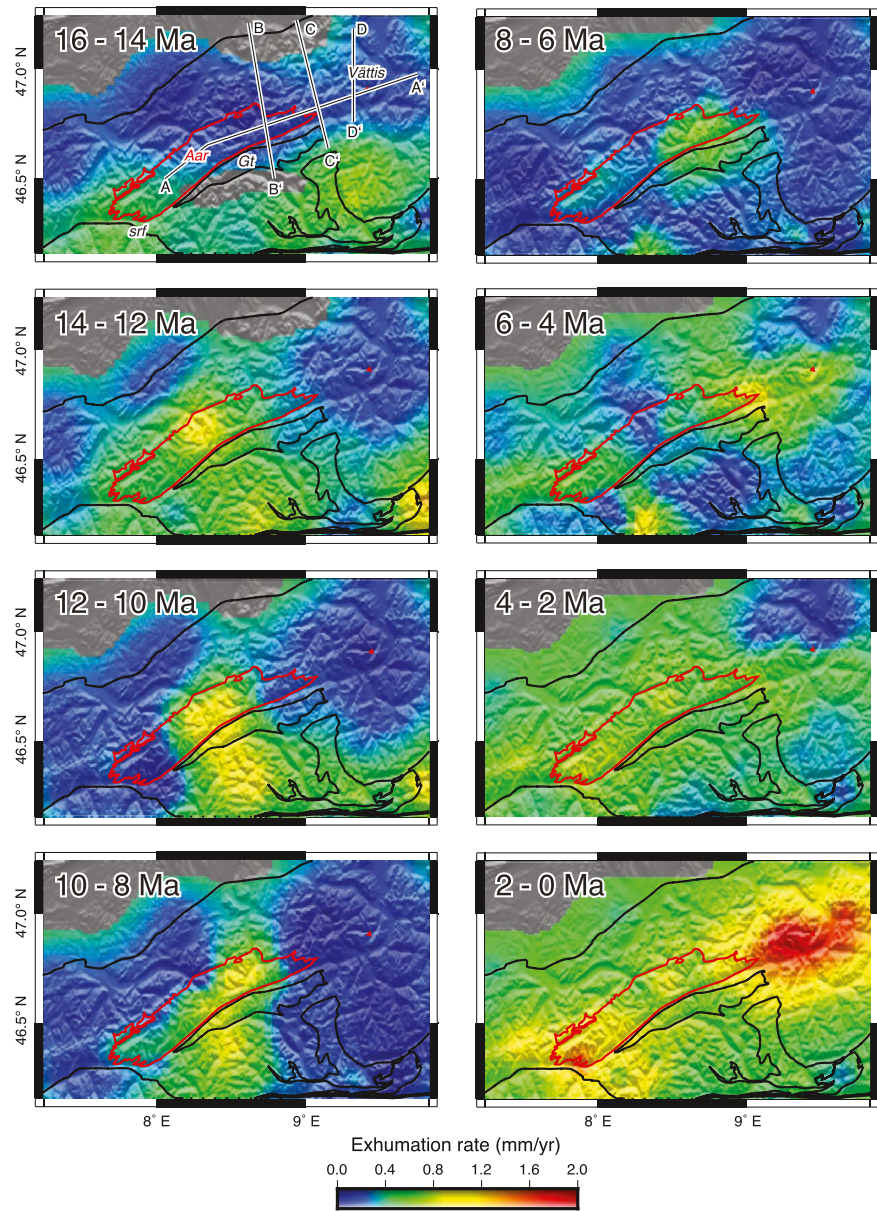


Figure 6. Calculated exhumation rates from 16 Ma to present for 2 Myr time steps based on the inversion of new and published thermochronometric data (references are given in the text). Section traces are highlighted as black lines in the top left sub-figure. The Aar Massif boundary and other tectonic boundaries are highlighted with red and black lines, respectively. Abbreviations as on Figure 1.

3.3. Inversion Model Setup and Parameters

In a late-stage orogenic setting such as the Neogene European Alps with estimated convergence rates no higher than 2 mm/yr (Schmid et al., 1996), cooling ages may to a first order reflect exhumation. In such a setting, in situ heat production or thermal relaxation after peak metamorphism may not have a significant impact on the cooling ages. Hydrothermal activity (Valla et al., 2016) or infiltration of meteoric water (Aronst, 2016) may lead to short-lived and local thermal anomalies, but cannot explain the overall smooth age distribution at the scale of the Aar Massif (Figure 3). In the inversion model approach we apply, cooling ages are assumed to reflect exhumation.

For the quantitative assessment of exhumation rates in space and time, we applied an inversion method on new and compiled ZFT, ZHe, AFT, and AHe ages. This inversion method was first established by Fox

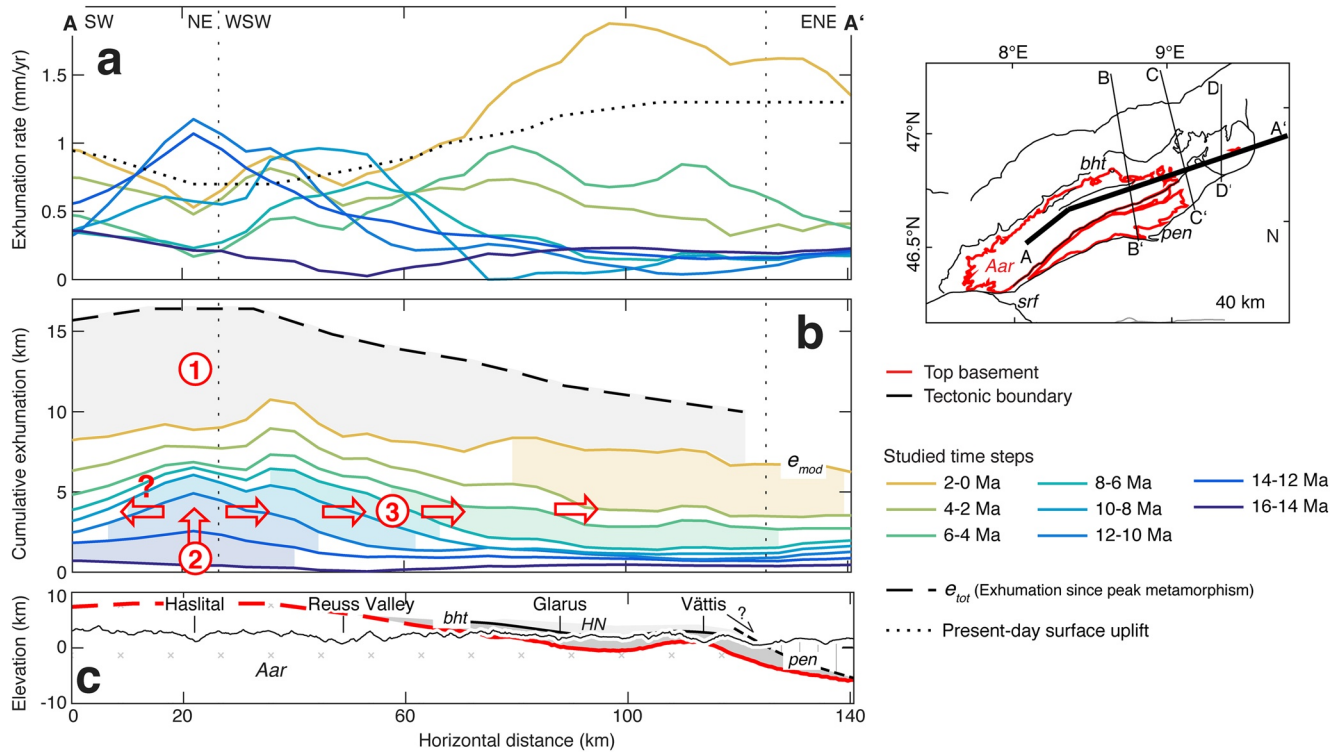


Figure 7. (a) Modeled exhumation rates, present-day surface uplift rates (Schlatter, 2014) and (b) cumulative exhumation calculated for 2 Myr time steps over the past 16 Ma along section A-A'. Regions of accelerated exhumation are shaded. The total exhumation since Alpine peak temperature conditions is inferred from depth-converted peak metamorphic temperature data (Figure 2). The red “1” highlights early exhumation from the moment of peak metamorphic conditions to 16 Ma (gray area). Red “2” highlights the rapid exhumation restricted to the central Aar Massif from 16 to 10 Ma. Red “3” highlights eastward migration of exhumation from 10 Ma to present. (c) Structural relief and major detachments along section A-A'. Legend and abbreviations as on Figure 1.

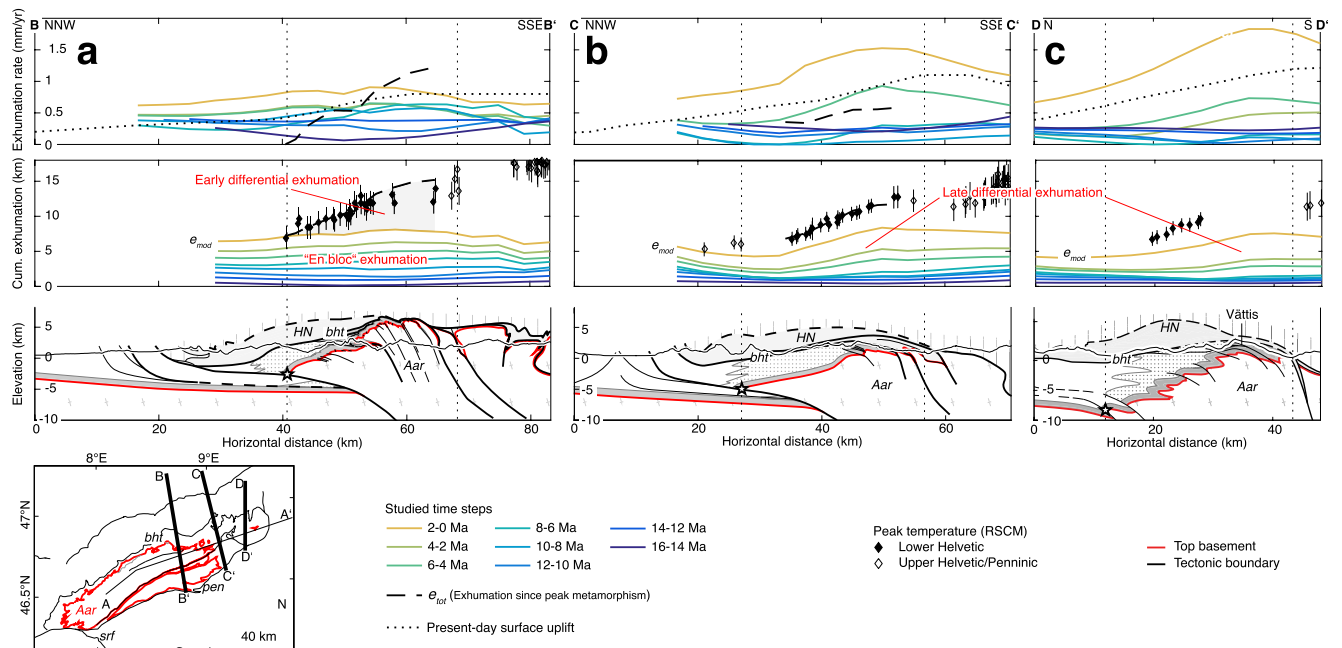


Figure 8. Inverse model results plotted along (a) cross section B-B', (b) cross section C-C', and (c) cross section D-D'. See Figure 7 for explanations. Legend and abbreviations as on Figure 1. References to peak temperature data are given in Figure 2. The asterisks and the thin dotted black lines indicate the northern front of the Aar Massif. Present-day surface uplift rates are from Schlatter (2014).

et al. (2014) and Fox et al. (2015). We used here an updated version, which is described in Herman and Brandon (2015). The method exploits ages from multiple thermochronometric systems, distributed in space. We only considered ages younger than 30 Ma for our calculations.

Quantifying the closure depth z_c requires an estimate of the thermal structure in the crust at a given time in the past. This thermal structure can be perturbed mainly by two processes: (a) topography representing the external boundary condition and (b) heat advection due to exhumation (e.g., Fox et al., 2016). In this method, the closure depth z_c is described as the integral of the exhumation rate $\dot{\epsilon}$ from a given cooling age τ to the present (e.g., Stalder et al., 2020). The model assumes one simple exhumation event and is not able to capture reburial (i.e., negative exhumation rates). To avoid negative exhumation rates, this equation is thus translated to a logarithmic space:

$$z_c = \int_0^\tau \dot{\epsilon} dt \rightarrow \zeta = \ln\left(\int_0^\tau \exp(\epsilon) dt\right), \quad (1)$$

where $\zeta = \ln(z_c)$ and $\epsilon = \ln(\dot{\epsilon})$.

Using a flux bottom boundary condition, the thermal structure of the crust was estimated as a function of heat advection and topography. This way, geothermal gradients and cooling histories were calculated for each time step. The closure depth was derived from the thermal histories.

This inverse problem was then solved using the nonlinear least-squares method (e.g., Tarantola, 2005). To achieve this, the integral in Equation 1 was first discretized into fixed time intervals Δt :

$$\zeta = \ln\left(\sum_{i=0}^{\tau} \exp(\epsilon_i) * \Delta t\right), \quad (2)$$

As a next step, we imposed a spatial correction of ϵ by defining an a priori model covariance matrix C_M (Fox et al., 2014; Stalder et al., 2020). C_M contains the horizontal distance d between the i th and j th data points, and a Gaussian correlation function for each time interval Δt :

$$C_M(i, j) = \sigma^2 \exp\left(-\left(\frac{d}{L}\right)^2\right), \quad (3)$$

where L represents the correlation length scale and σ^2 is the a priori variance, which mainly serves as a weighting factor (Stalder et al., 2020). This way, the calculated exhumation rates are spatially correlated within a given distance but free to vary through time, which results in a smooth distribution, regardless of major detachments (e.g., Fox et al., 2014). Since both the calculations of the closure depth and the thermal structure depend on the erosion rate estimated by the model (Fox et al., 2014), a second nonlinear problem has to be solved using the steepest descent algorithm (Tarantola, 2005).

$$\epsilon_{m+1} = \epsilon_m - \mu(C_M G^T C_D^{-1}(\zeta_m - \zeta_{obs}) + (\zeta_m - \zeta_{prior})), \quad (4)$$

where m is the iteration number, ζ_{prior} the logarithm of the value chosen as a priori erosion rate $\dot{\epsilon}_{prior}$, C_D is the data covariance matrix, μ is an arbitrarily chosen parameter which controls how rapidly the model parameters evolve, ζ_m and ζ_{obs} represent the logarithms of the modeled and observed closure depths and G represents the derivative of $\ln(\sum_{i=0}^{\tau} \exp(\epsilon_i) * \Delta t)$ with respect to ϵ (Herman & Brandon, 2015; Stalder et al., 2020).

A list of input parameters is given in Text S6 in Supporting Information S1. Fifteen time intervals of 2 Myr between 30 Myr and present were used by the model. Given the spatial and temporal resolution of ages, reliable results can be shown for the 8 last 2 Myr time steps between 16 Myr and present. Therefore, the pre-16 Myr time steps are not shown in the results section. An a priori value for $\dot{\epsilon}_{prior}$ of 0.6 ± 0.3 km/Myr was chosen. This value represents the mean exhumation rates in the Alps since 35 Ma, which is based on the sedimentary record (e.g., Bernet et al., 2001; Glotzbach, Bernet, & van der Beek, 2011). We assume an undisturbed initial prior geothermal gradient G_0 of 20°C/km. This value is close to independent pressure temperature estimates from the study area (Challandes et al., 2008; Goncalves et al., 2012) and reflects the spacing between peak metamorphic isograd surfaces in Wiederkehr et al. (2011). The model was run with a correlation distance of 20 km (see also Text S6 in Supporting Information S1).

The input parameters G_0 , $\dot{\epsilon}_{prior}$, and the 30 Myr model run time define the final geothermal gradient (33°C/km) at the end of the prior model. This value is close to the ~30°C/km estimated from surface heat flux

data across the study area (Bodmer & Rybach, 1984). These data are, however, relatively old and poorly constrained by only a relatively small number of borehole or tunnel data.

$\dot{\epsilon}_{prior}$ influences all time steps of the model, because it remains part of the solution (see Equation 4, Jiao et al., 2017; Willett et al., 2020). This influence is more pronounced when the data have a poor temporal or spatial resolution, which is not the case in our study area. Given the coupling between the geothermal gradient and exhumation rate also G_0 influences the model results. For example, assuming a high prior geothermal gradient leads to more shallow closure depths. As a consequence, our model predicts lower exhumation rates. Therefore, a sensitivity analysis was performed for G_0 ranging between 15 and 30°C/km. To test the model sensitivity, we performed additional model runs for $\dot{\epsilon}_{prior}$ values of 0.4, 0.8, and 1.0 km/Myr, respectively. These values represent the estimated minimum and maximum exhumation rates over the past 20 Myr in the study area (Glotzbach et al., 2010; Nibourel et al., 2021; Vernon et al., 2008).

The model calculates an average transient geotherm from a 1-D solution to the advection-diffusion equation for heat transfer to an isothermal boundary condition at the Earth's surface, which is set to 15°C (at 0 m elevation, see also Text S6 in Supporting Information S1). This value is arbitrarily chosen and has little influence on the modeled exhumation rates. Nevertheless, paleo climate reconstructions (e.g., Zachos et al., 2001) indicate that the value chosen represents a realistic estimate of the mean temperature value over the past 30 Myrs. The model operates with a thermal thickness of 50 km, which corresponds to the crustal thickness below the central Alps (Schmid et al., 1996). The advective term in the heat equation is determined using the above a priori values G_0 and $\dot{\epsilon}_{prior}$. The thermal diffusivity of 30 km²/Myr used in the model is in agreement with heat flow data from the study area (Bodmer & Rybach, 1984).

The closure temperature and cooling rate (at the time equivalent to the cooling age) for a specific thermochronometric age is updated during the optimization of the exhumation model (Fox et al., 2014). To update the closure temperature, the model uses the annealing/diffusion kinetic parameters given in Reiners and Brandon (2006), assuming the conventional cooling rate of 10°C/Myr.

The calculation of the temperature perturbations downward from the topographic surface required (a) a 90 m digital elevation model (Jarvis et al., 2006), (b) an estimate of the atmospheric lapse rate (6°C/km), and (c) the determined geotherm, which is derived from the average transient solution for the relevant time (Fox et al., 2016). Using a spectral method, temperature perturbations were then extended downwards to the depth of interest (Fox et al., 2016; Mancktelow & Grasemann, 1997; Stüwe et al., 1994). Finally, this perturbation in temperature was converted to a perturbation of a given closure depth isotherm using the transient geotherm calculated for the relevant time. The model assumes a stationary topography over time (Fox et al., 2014). This is in agreement with Campani et al. (2012) and Schlunegger and Kissling (2015) who found evidence for a relatively constant topography of the Alps since the Miocene.

The reliability of the solution was assessed by computing the reduced variance (the ratio between the a posteriori and a priori variance, Fox et al., 2014, see Figure S1 in Supporting Information S1). At a temporal or spatial resolution of cooling ages close to 0, calculated exhumation rates will not significantly deviate from the a priori value of 0.6 km/Myr. Values close to 1 indicate that our solution was defined and improved by a high number of thermochronometric constraints.

4. Results

4.1. Thermochronometric Ages

New ZFT, AFT, and ZHe ages are summarized in Table 1. Detailed information on the ages can be found on Tables S2–S6 in Supporting Information S1, track length data (only available for key samples) for the ZFT and AFT ages are shown in Tables S7 and S8 in Supporting Information S1. New and published ages are shown in map view (Figure 3), along a transect parallel to the massif (Figure 4) and along three transects perpendicular to the massif (Figure 5).

New ZFT ages >30 Ma are mostly situated at the northern border of the Aar Massif. These ages are older than the the age of Alpine peak metamorphism in the Lower Helvetic and were not reset during the Alpine orogeny (Figure 5). Further south, ages are generally <30 Ma and were at least partially reset during the Alpine cycle. Alpine reset ZFT ages cluster between 8.7 and 13 Ma (Figures 4 and 5). ZFT track lengths (only

available for key samples) are in the order of 7.7–10.6 μm (see Table S7 in Supporting Information S1). In three out of six young (<30 Ma) ZFT ages, track lengths >10 μm and a unimodal track length distribution (Tagami et al., 1998) point to a complete reset (Table S7 in Supporting Information S1). In contrast, the presence of short tracks in the relatively young ZFT age from the Vättis window (MRP169, 10.4 Ma) suggests no complete reset in these zircons.

The youngest AFT ages (1.6–7 Ma) are found in the Vättis window. Samples from the Helvetic nappes yielded AFT ages up to 20 Ma. Dpar values range from 1.38 to 2.26 μm (Table S3 in Supporting Information S1) and highlight the presence of fluorine- and chlorine-bearing apatites, thus indicating nonuniform annealing kinetics. However, Dpar values of all key samples along the strike of the Aar Massif are fluorine-rich (Dpar <1.75 μm). Hence, the age increase from the eastern to the central Aar Massif does not reflect compositional variation. AFT track lengths (>14 μm , Table S8 in Supporting Information S1) indicate fast cooling in the Vättis window, decreasing toward the central Aar Massif and toward the north (see Figure 3, Vernon et al., 2008). Fast post-6 Ma cooling in the Vättis area is also confirmed by an inverse relationship between AFT ages and associated mean track lengths (Rahn, 2001).

New ZHe ages range between 6 and 27 Ma and are mostly younger than associated or nearby ZFT ages (Table 1). ZHe ages >13 Ma are restricted to the Lower Helvetic sediments north of the Aar Massif (Figure 5) and are characterized by a relatively large spread of single grain ages (see also Tables S4–S6 in Supporting Information S1). In the central Aar Massif, ZHe ages are between 7 and 11 Ma without clear age trends (Figures 4 and 5). Errors (1σ) do not exceed ± 1.2 Ma. In the eastern Aar Massif, ages range between 8 and 6.5 Ma. The youngest age (6 ± 0.6 Ma, sample MRP169) was reported in the Vättis window (Figure 4). Two samples from the Helvetic nappes yielded ages of 26.1 and 8.9 Ma, respectively. ZHe ages with weakly negative eU-age relationship are restricted to areas of higher Alpine metamorphic overprint (peak temperature >330°C, Figure 2), thus suggesting relatively weak radiation damage. Four single ages were, given their age which is older than the onset of burial (~30 Ma) estimated for the Lower Helvetic, identified as unreset and therefore rejected for the calculation of the unweighted mean sample age (see Tables S4–S6 in Supporting Information S1).

4.2. Isoage Maps

Figure 3 shows new and published ZFT, ZHe, and AFT ages together with inferred isoage contour lines for the 1,500 elevation level. Elevation-corrected ZFT ages show a decrease from ~15 Ma in the central southern Aar Massif to 10 Ma in the Vättis window. The 20 Ma isoage line closely follows the northern boundary of the central Aar Massif and is situated close to the northern end of the reset zone. Isoage lines are oblique to major tectonic boundaries such as the Urseren-Garvera zone. A zone with ages <10 Ma coincides with the Vättis area and with the eastern Gotthard nappe.

Elevation-corrected ZHe ages gently decrease from an average value of 10 Ma in the central Aar Massif to 6 Ma in the Vättis window (Figures 3 and 4). Ages increase rapidly north of the Aar Massif. The region with the youngest ZHe ages extends into the Penninic domain southeast of Chur (Figure 3). From Chur, ages increase toward the south and east. The area north to the Vättis window is not covered by ZHe data.

In the central Aar Massif, elevation-corrected AFT ages range between 6 and 8 Ma. The youngest AFT are situated in the Vättis window and increase toward the central Aar Massif. A concentric area with the youngest ages is aligned with the easternmost exposure of the Aar Massif. No significant jump in ages is observed across major detachments such as the basal Helvetic thrust or the Penninic front (Figure 3). We interpret the rapid increase of ZFT and ZHe cooling ages toward the north and partially toward the east to reflect variations in the metamorphic overprint (Figure 2). Ages from this zone are considered not completely reset. In contrast, age variations within the reset zone, such as the systematic decrease of all cooling ages from the central Aar Massif toward the Vättis window, are likely to reflect a different timing or rate of cooling.

4.3. Age Constraints on Deformation

Figures 4 and 5 highlight the surface topography and the distribution of cooling ages along a cross section parallel and three published cross sections perpendicular to the massif (Nibourel et al., 2018; Pfiffner, 2011).

In along-strike direction (Figure 4), top basement descends from an estimated elevation of 7 km in the central Aar Massif to an elevation <1 km east of the Vättis window with a mean axial plunge of 5–10° (Herwegh et al., 2020; Hitz & Pfiffner, 1994; Nibourel et al., 2018). In orogen-perpendicular direction, top basement increases from an elevation of –6 km in the footwall of the Alpine sole thrust (Pfiffner et al., 1997) to approximately 7 km at the crest of the Aar Massif, then comes back down to sea level south of the Aar Massif (Pfiffner, 2011), which corresponds to an amplitude of up to 12 km (Figure 5, cross section B-B'). This amplitude decreases to less than 9 km along cross section D-D' (Figure 5). The present-day geometry of top basement serves as an independent proxy for the integrated amount of exhumation since the time top basement was gently dipping in southward direction prior to the Aar Massif uplift (Nibourel et al., 2018).

As highlighted on Figure 4, the ages decrease from the central Aar Massif to the Vättis window. The youngest ZFT, ZHe, and AFT ages are situated at the easternmost exposure and not in the center of the massif. In contrast, the exposed metamorphic grade (Figure 2) and the present-day structural relief (Figures 1 and 5c) highlight that total exhumation was overall largest in the central southern Aar Massif. This suggests that most of the dome shape of the Aar Massif shown on Figure 5 developed between the time of peak metamorphic conditions at ~22–17 Ma and the closure of the ZFT system at 10–15 Ma.

Distinct changes in the age pattern also occur perpendicular to the massif (Figure 5). Along the Reuss Valley transect, elevation-corrected and Alpine reset ZFT, ZHe and AFT ages are relatively constant (Figure 5, left). No significant ZFT age jump is observed between the Aar Massif and the Gotthard nappe, indicating the absence of significant differential vertical movements between the two tectonic units after the closure of the ZFT system at ~13–15 Ma (Glotzbach et al., 2010; Peters, 2012). Near-constant ZHe and AFT age patterns do not reflect the dome structure and associated major faults in the internal parts of the massif (Figure 5). This suggests that this part of the Massif exhumed with minor internal differential vertical movements (“en bloc”) at least since the closure of the ZHe system at ~9–11 Ma. As a consequence, the structural relief and associated reverse faults in the internal parts of the massif must have developed earlier.

In contrast, clear age trends are observable along the Glarus and Vättis transects (Figure 5, centre and right). In the Vättis transect, the youngest AFT ages coincide with the crest of the eastern Aar Massif and ages increase particularly to the north but also to the south (Figure 5). Although less pronounced, the same age pattern can be recognized along the Glarus transect (Figure 5, see also Rahn et al., 1997). This points to continued development of the structural relief after AFT closure between ~10 and 2 Ma.

4.4. Exhumation Rates in Space and Time

Inverse modeling results are presented in the form of an array of maps. These maps show the evolution of exhumation rates for the past 16 Ma for 2 Myr time steps (Figure 6). Figure S1 in Supporting Information S1 shows a high temporal resolution of model input data, especially for the Lower Helvetic domain from 14 Ma to present. This corroborates the reliability of our model observations.

Figures 7a and 8a show the modeled exhumation rates along the four studied transects. On the same figures, exhumation rates for each time step multiplied by time (2 Myr) are cumulatively plotted to add up to the modeled sum of exhumation from 16 Ma to present, in the following referred to as e_{mod} (Figures 7b and 8b). Exhumation has likely initiated earlier, but is poorly constrained by cooling ages. As a consequence, e_{mod} does not represent the total amount of exhumation, but rather the time interval for which model results yield a sufficiently good spatial and temporal resolution. Therefore, complementary to the model results, an approximation of the total exhumation (e_{tot}) is shown in Figures 7b and 8b. It is inferred from Alpine peak temperature data converted to paleo depth at the time of peak temperature conditions, assuming a constant geothermal gradient of 25°C/km at peak temperature conditions (at ~17–22 Ma in the central Aar Massif, Nibourel et al., 2018).

The assumed geothermal gradient is comparable to the average transient geotherm calculated by the inverse model for that time, which is a requirement for the comparison of the two data sets in Figures 7b and 8b. Furthermore, the assumed geothermal gradient is in agreement with the spacing of peak temperature isograd surfaces in the study area (Nibourel et al., 2021) and with independent pressure temperature time constraints (Challandes et al., 2008; Goncalves et al., 2012; Rolland et al., 2009). Peak metamorphism

in the Lower Helvetic domain is due to the burial in the footwall to the basal Helvetic thrust, representing the main active tectonic boundary at that time (Pfiffner, 2015). According to numerical models (Shi & Wang, 1987), temperature perturbations across shallow-dipping active thrusts with slip rates no higher than 5 mm/yr, such as the basal Helvetic thrust, re-equilibrate rapidly (Nibourel et al., 2021; Pfiffner, 2015) so that the assumption of a constant geothermal gradient of 25°C/km appears justified for this time step, even if minor temperature perturbations cannot be excluded.

The inverse model allows temperature gradients to vary through time and in space (Fox et al., 2014). The 25°C/km gradient we applied to convert peak temperatures to depth is thus not necessarily equivalent to the temperature gradient calculated by the inverse model at that given time at a given locality. Hence, absolute differences between e_{tot} and e_{mod} have to be considered with caution.

Calculated exhumation rates highlight a distinct space-time evolution, especially along the strike of the Aar Massif. Between 16 and 10 Ma, maximum rates of up to 1 mm/yr are situated in the central Aar Massif while the eastern Aar Massif exhumes at much slower rates (<0.5 mm/yr, Figure 6, see also vertical red arrow labeled with a “2” on Figure 7). From 10 Ma onwards, maximum exhumation rates progressively migrate in orogen-parallel direction, from the central to the eastern Aar Massif, reaching the Vättis area at ca. 6–2 Ma (see horizontal red arrows labeled with a “3” on Figure 7).

Exhumation rates do also vary in the direction perpendicular to the massif (Figures 6 and 8). Along the Reuss Valley transect, exhumation rates are relatively constant through the past 16 Ma (see “en bloc” exhumation in Figure 8a). In contrast, model results highlight differential exhumation with its maximum near the crest of the eastern Aar Massif from 8–6 Ma to present (i.e., “late differential exhumation” on Figures 8b and 8c).

From 2 Ma to present, the model results show a twofold increase of exhumation rates affecting the study area at a larger scale. However, the spatial distribution of exhumation rates is consistent with the pre-2 Ma evolution (i.e., eastward-migration of exhumation, see Figure 6).

The cumulatively plotted model results on Figures 7 and 8 illustrate the progressive exhumation of a hypothetical initially horizontal marker through the past 16 Myrs. The difference between e_{mod} and e_{tot} highlights the amount of exhumation between peak temperature conditions and 16 Ma (i.e., gray areas on Figures 7b and 8a). Our results demonstrate that a large amount of the west-east structural relief developed prior to 16 Ma (i.e., “early exhumation” highlighted with a red “1” on Figure 7b). Along the Reuss Valley transect, the structural relief in the internal parts of the massif must have developed prior to 16 Ma (i.e., “early differential exhumation” on Figure 8a, left). From 16 Ma onwards, the model predicts nonsteady but spatially uniform “en bloc” exhumation (Figures 8b and 8c). Along the Glarus and the Vättis transects, e_{mod} and e_{tot} reflect the present-day geometry of top basement (Figures 8b and 8c). In contrast to the central Aar Massif, this points to continued differential rock uplift in the eastern Aar Massif after 6 Ma.

Along the Reuss Valley transect, average modeled exhumation rates of ca. 0.5 mm/yr are in agreement with estimates by Glotzbach et al. (2010). However, pulses of faster exhumation from 16 to 14 Ma and from 10 to 7 Ma as proposed by Glotzbach et al. (2010) were not reproduced by our model results. This could be due to the 2 Myr time step used in our model, which might be too large to resolve pulses of relatively short duration. Along the Glarus transect, our results highlight differential exhumation and an associated ~7° northward tilting after ca. 8 Ma, north of the underlying Aar Massif (Figure 8b). The post-2 Ma acceleration of exhumation rates in the Vättis region is consistent with a similar increase since 3 Ma found by Vernon et al. (2008) and Fox et al. (2016).

In order to test the robustness of the model observations, we evaluated the influence of the following key input parameters on the key observations: (a) the a priori exhumation rate, (b) its uncertainty, and (c) the correlation distance (Fox et al., 2014; Herman & Brandon, 2015). Exhumation patterns and their space time evolution, including the migration of peak exhumation in along-strike direction, were stable features through the sensitivity analysis, thus confirming the robustness of our first order observations.

In the inverse model, the closure depth of a specific cooling age at the time equivalent to the cooling age is calculated based on the present-day topography. Changes in position of valleys and peaks or in the overall topography in the past cannot be predicted by the model but could influence our results, especially the

calculated closure depths of AFT and AHe data. Closure temperatures $>200^{\circ}\text{C}$ are not significantly influenced by topography (Mancktelow & Grasemann, 1997). Additionally, rates calculated for the time interval between the closure of the last thermochronometer and present might vary as a function of the assumed rock temperature at surface. Therefore, the post-2 Ma signal has to be interpreted with caution. Another limitation of the used inversion method is the assumption of a purely vertical exhumation path of the rock toward the surface. Nibourel et al. (2018) estimated a ratio of vertical uplift to shortening >0.7 for the exhumation of the central Aar Massif. Hence, particle paths had a horizontal component. This cannot be captured by the model but could potentially influence the thermal history in the area. Furthermore, heterogeneous retention and annealing kinetics in apatites and zircons, as well as heat conductivity variations between the sedimentary cover and crystalline basement are not considered by the model.

4.5. Independent Kinematic and Age Constraints From Exposed Fault Zones

Overall, independent kinematic and age constraints from exposed shear zones are in good agreement with thermochronometry-based modeled exhumation dynamics. This corroborates our model results and points to a strong link between basement-involved crustal thickening and exhumation during the Neogene.

Our thermochronology-based results (Figure 8a) suggest that most of the deformation in the internal parts of the central Aar Massif developed after the thermal peak (22–17 Ma) and prior to ZFT closure at ca. 16–14 Ma. This is in agreement with the 21–17 Ma age of an early set of steep ductile reverse faults with mostly S-block up kinematics in this area (see Section 2.1 for details). The early exhumation with simultaneous differential N-S rock uplift in the internal parts of the central Aar Massif (including the Reuss Valley transect, “early differential exhumation” in Figure 8a) can thus be attributed to these early reverse faults.

The transition from compressional to transpressional tectonics at 14–10 Ma provides a good explanation for the absence of significant N-S differential exhumation in the internal parts of the massif along the Reuss Valley transect (Figure 8a) from 14 Ma onwards (see Section 2.1 for details). Our thermochronometry based results highlight no significant gradient in the exhumation rates across the central Aar Massif between 16 Ma and present, in the following referred to as “en bloc” exhumation (Figures 7b and 8a). This spatially uniform exhumation rates may reflect “en bloc” exhumation in the hanging wall of frontal crustal ramps, such as the exposed Pfaffenchof thrusts (see Section 2.1 for details).

4.6. Earthquake Data

Recent seismicity gives additional insights regarding the distribution and kinematics of deformation over the past decades. Figure 9 shows available earthquake focal mechanisms for the study area, colored for distance to top basement (Deichmann, 2014; Diehl et al., 2014, 2015, 2018; Kastrop et al., 2004; Marschall et al., 2013). The estimated uncertainty related to the focal depths is ≤ 3 km for high-quality hypocentral solutions, but could be larger for lower quality localizations (for details on quality assessment of focal depth uncertainties, see Deichmann et al., 2000; Diehl et al., 2014). A cluster of earthquakes indicating thrust tectonics can be identified north of the Vättis area (marked by black arrows on Figure 9). Most of these earthquakes occurred at relatively shallow depths and associated hypocenters are situated close to the top basement horizon (Persaud & Pfiffner, 2004). Two clusters of strike-slip dominated earthquakes are observed in the Glarus area and between Feldkirch and Chur (Figure 9). Many of these events might be located within the basement, or within the Lower Helvetic sediments.

Seismic activity in the Penninic domain south of Chur is characterized by normal faulting, indicating southwest-northeast extension. Given the very low convergence rates between Europe and Adria, the seismic record (covering the period from 1984 to 2018) represents a very short time interval and associated interpretations should be considered with caution. Although the seismicity in the Helvetic domain is overall dominated by E-W and N-S strike-slip faulting, we observe an increased tendency to compressional tectonics, which coincides with the approximate position of the Alpine sole thrust (Figures 1 and 9, Pfiffner, 2011) and with the region of most rapid and differential post-2 Ma exhumation in the hinterland (see highlighted area around Vättis on Figure 9). Regions for which our model calculates comparatively low post-2 Ma exhumation rates, such as the central Aar Massif (Figure 6), are characterized by low seismic activity including strike-slip and/or normal faulting (Figure 9).

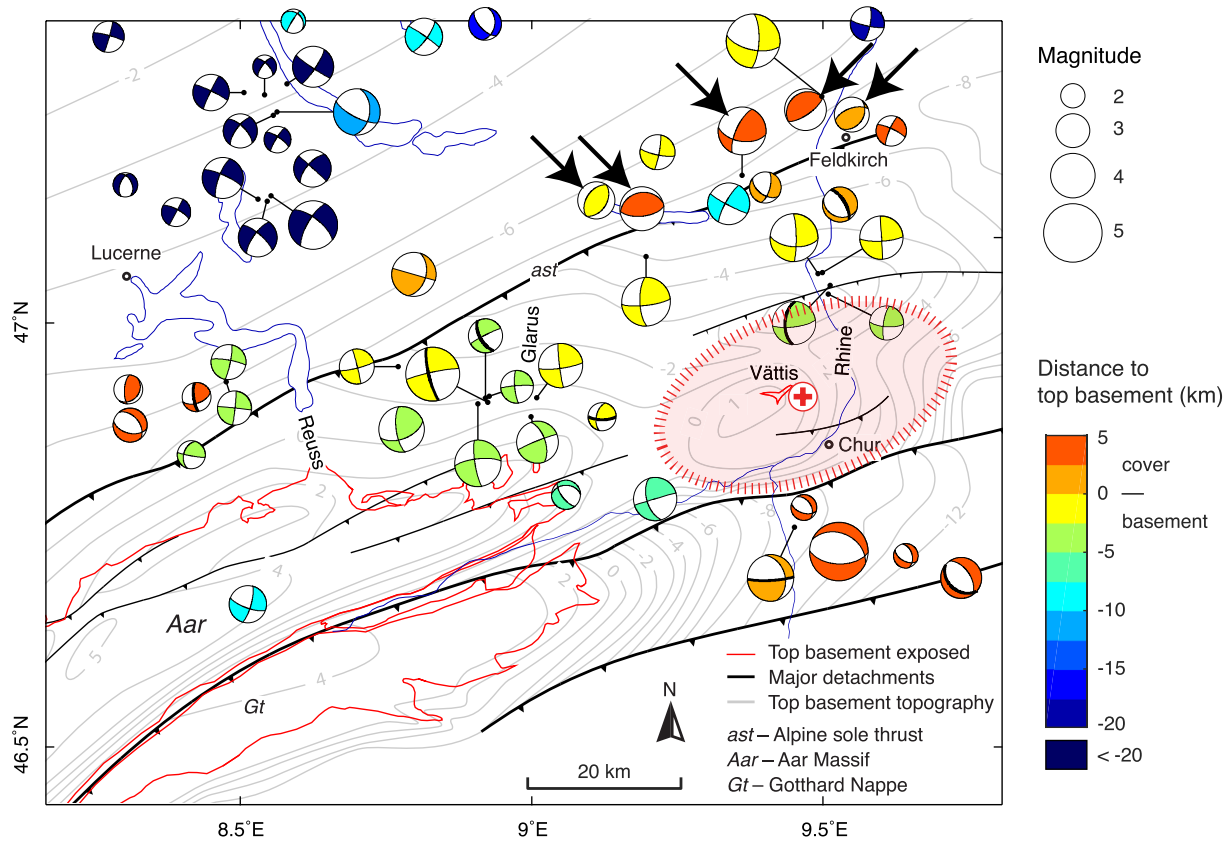


Figure 9. Compiled earthquake focal mechanisms in the study area, colored after distance to top basement for the years 1984–2018 (see text for references). Where identified, fault planes are highlighted as bold black lines. Top basement topography (shown as gray contour lines in the background) including major detachments (at the level of top basement) are from Pfiffner (2011). The Aar Massif exposure is outlined by a solid red line. Black arrows highlight thrust-related earthquakes north of the Vättis area, the region of maximum post-2 Ma exhumation rates (red ellipse with dashed outline).

5. Discussion

5.1. Kinematic Scenario for Noncylindrical Orogen-Parallel Massif Growth

Our results highlight a noncylindrical evolution of the Aar Massif associated with eastward migration of exhumation in an orogen-parallel direction, and thus perpendicular to the overall north-northwest trending transport direction in the Helvetics (e.g., Pfiffner, 2011). We propose a kinematic scenario for the development of the Aar Massif in which exhumation is mainly driven by compressional tectonics (Figures 10 and 11). In the central Aar Massif, the scenario is well constrained by independent thermochronometry and field constraints. In the east, the distribution of basement shear zones is poorly known and our interpretation has to be considered with caution. Possible positive feedback mechanisms with erosional processes are addressed below. Schematic tectonic sketch maps on Figure 10 illustrate the structural evolution for three time intervals. Likely active faults and associated regions with maximum exhumation are highlighted for each time interval. The schematic 3D sketches on Figure 11 illustrate the active faults and the associated development of the structural relief as well as the resulting exhumation signal for the same three time intervals.

1. 22–16 Ma: Shortening and crustal thickening in the basement first initiated in the central southern Aar Massif. We correlate this early phase of rapid and differential exhumation with the exposed east-north-east-striking and steeply south-southeast dipping to sub-vertical reverse faults and with a pervasive greenschist facies foliation (Figure 10, “Reverse faults” on Figure 11, e.g., Herwegh et al., 2017; Rolland et al., 2009; Wehrens et al., 2017). This early phase produced (a) the structural relief as seen in the internal parts of the central Aar Massif (“early differential exhumation” on Figure 8a), and (b) the N-S metamorphic gradient (Figures 2 and 8a, Nibourel et al., 2018, 2021). In the Vättis area, our data (thermochronometric ages and peak temperatures) do not record significant exhumation during this period.

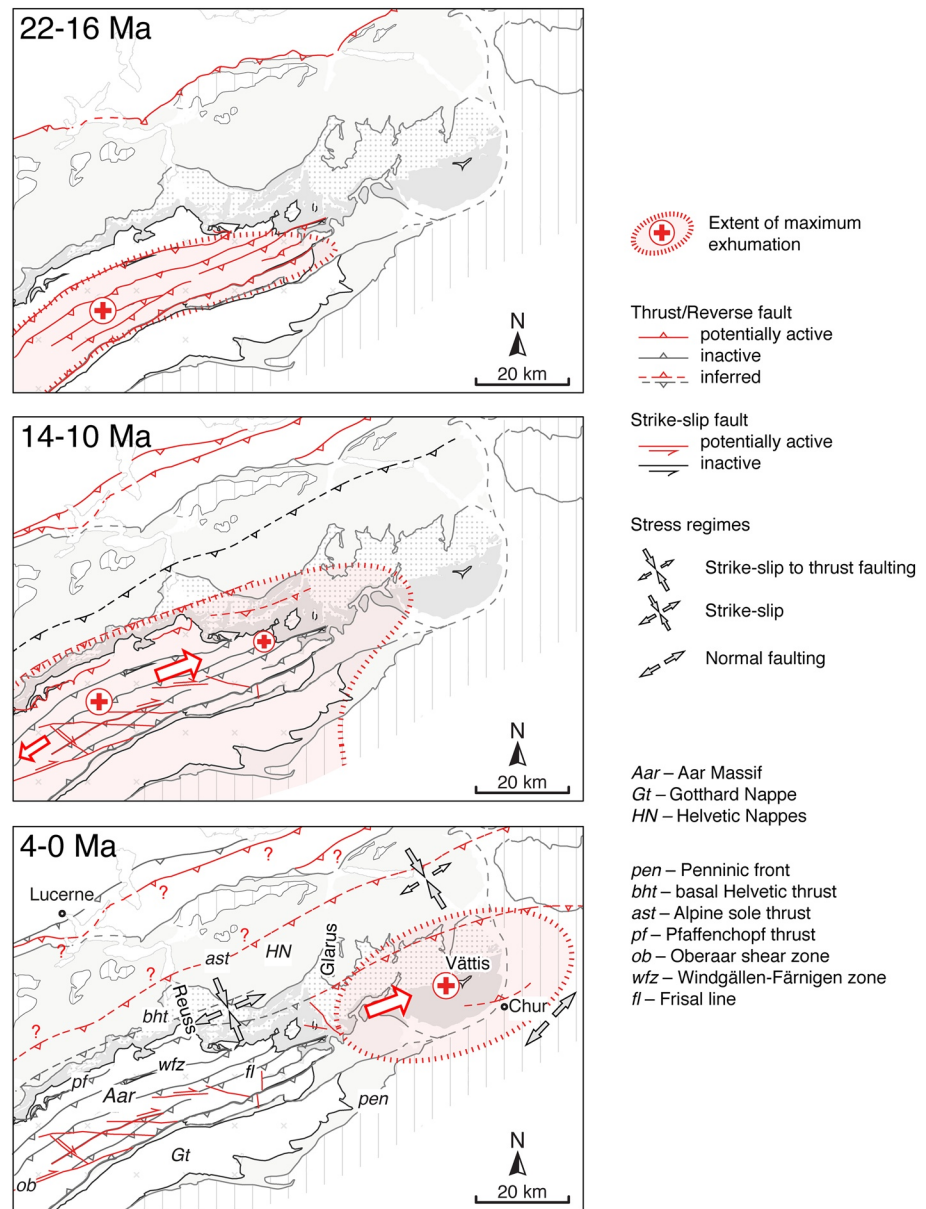


Figure 10. Schematic tectonic sketch maps illustrating the structural evolution and exhumation of the central and eastern Aar Massif (see text for references and discussion). Recent seismicity highlights an increased tendency to thrust faulting near the basement-cover interface in front of the Vättis area (stress regime symbols modified from Marschall et al., 2013). Red arrows highlight the orogen-parallel migration of exhumation initiating at ca. 10 Ma. Legend as on Figure 1.

2. 14–10 Ma: In the southern central Aar Massif, cross-cutting relationships and isotopic ages suggest a transition to transpressional tectonics with a dominant strike-slip component (Figure 10, “strike-slip faults” on Figure 11). Simultaneously, compressional deformation along the northern central massif-front progrades toward the North Alpine Foreland where new north-northwest-vergent crustal ramps/thrusts are activated (i.e., “frontal thrusts” on Figure 11), which correlates with imbricate thrusting in the Subalpine Molasse (Mock et al., 2020; von Hagke et al., 2012). Relatively rapid “en bloc” exhumation from ca. 14–10 Ma is observed in the hanging wall of these crustal ramps. The transition to strike-slip dominated tectonics explains the absence of differential exhumation in the southern central Aar Massif. From 10 Ma onwards, the focus of crustal thickening and exhumation migrates in an orogen-parallel and eastward direction toward the east corner of the massif. At ca. 8–6 Ma, the area of maximum crustal thickening and exhumation reaches the Glarus region where it causes tilting in the overlying Helvetic nappes (see Figures 7, 8b and 10, Rahn et al., 1997). At the same time, we observe a decrease of exhumation rates in the central Aar Massif.

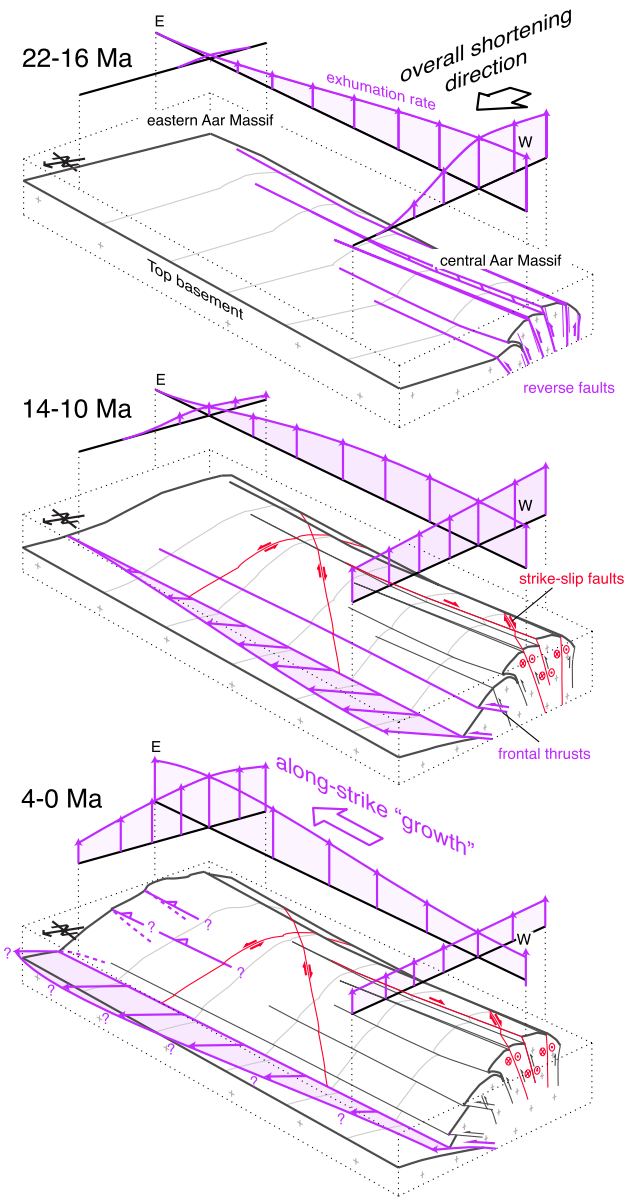


Figure 11. Schematic sketches showing the development of the Aar Massif (top basement) and the eastward migration of exhumation in orogen-parallel direction for the time intervals shown on Figure 10. Key structural elements such as reverse faults and frontal thrusts (purple) as well as strike-slip faults (red) are highlighted. Purple arrows indicate hypothetical displacement variations along these structures. Associated exhumation rates are shown for two transects perpendicular to the central and the easternmost Aar Massif (Vättis area) and along one axial transect. See text for discussion and references.

- 4 Ma to present: Our results highlight continued eastward migration of exhumation toward the present-day (Figures 10 and 11). Compared to the eastern Aar Massif, the central Aar Massif continues to exhume at slower rates. The good correlation between exhumation maxima and top basement highs in the Vättis area suggests that at least the pattern of exhumation is to a first order controlled by crustal thickening. However, exhumation rates above 1.5 mm/yr estimated for this time interval are equal or higher than present-day convergence rates (<1 mm/yr) and comparable to modern surface uplift rates up to 1.5 mm/yr (e.g., Sternai et al., 2019). Such high exhumation rates relative to slow convergence rates may result from positive feedback mechanisms between crustal thickening and efficient erosion of the sedimentary units overlying the Aar Massif, especially during the Quaternary glaciations (e.g., Seguinot et al., 2018). Interpreted faults in cross section D-D' (Figure 8) indicate multiple detachments with a fault dip increasing from N to S (Pfiffner, 2011). This interpretation was considered for our kinematic model on Figure 11, which is consistent with the cluster of thrust-related earthquakes north of the Vättis area (Figure 9).

In the above kinematic scenario, along-strike exhumation variations are linked to changes in the distribution or intensity of compressional deformation in the Aar Massif basement. This may be achieved (a) by displacement or dip variations along the strike of thrusts and reverse faults, (b) by laterally varying spacing of thrusts and reverse faults, or (c) by decoupling individual fault segments by transverse faults. There is some field evidence for large displacement variations, for example along the strike of the Windgällen-Färnigen zone (Figure 10, Nibourel et al., 2018, 2021) and the Frisal line (Figure 10, Pfiffner, 1978). Both reverse faults appear to die out laterally, but in opposite directions (Nibourel et al., 2021). An overall change in the spacing of faults from the central to the eastern Aar Massif is not observed (Baumberger, 2015; Nibourel et al., 2021). In contrast there is some field evidence for transform faulting. The most prominent examples, from west to east, are the Oberaar fault zone (Belgrano et al., 2016; Egli et al., 2018; Rolland et al., 2009; Wehrens et al., 2017), the Panixer Pass transverse zone (e.g., von Däniken & Frehner, 2017), or the Kunkels Pass transverse fault (Pfiffner, 1972). The presence of transverse faults is also indicated by strike-slip dominated recent seismicity in the Helvetics (Figure 9, Deichmann, 2014; Diehl et al., 2014, 2015, 2018; Kastrup et al., 2004; Marschall et al., 2013).

5.2. Present-Day Situation

Although the two-fold increase of exhumation rates between 2 Ma and present predicted by the model has to be considered with caution, it is consistent with other studies (e.g., Vernon et al., 2008) and with inde-

pendent geodetically derived present-day surface uplift rates (see dotted black lines in Figures 7a and 8, Schlatter, 2014). This suggests that at least the predicted pattern of exhumation rates represents a meaningful result.

The position of the concentric post-2 Ma exhumation peak centered around the Vättis window represents the logic continuation of the eastward migration of exhumation—a process that, according to our results,

initiated at ca. 10 Ma. This suggests that compressional deformation and crustal thickening, although at relatively slow rates, might still be active processes especially in the easternmost Aar Massif.

Some evidence for continued compressional tectonics is also found in the recent seismic activity. Focal mechanisms in the Aar Massif/Helvetic domain are overall dominated by strike-slip. However, an increased tendency to thrust-faulting can be observed in the vicinity of the Alpine sole thrust north of the most rapidly exhuming Vättis area (Figure 9). The comparatively slow post-2 Ma exhumation rates in the central Aar Massif are reflected by moderate seismic activity, dominated by strike-slip or normal faulting (Figure 9).

Given the slow (<1 mm/yr) present-day convergence rates (Sternai et al., 2019) estimated for the eastern Aar Massif, tectonic processes alone are unlikely to explain the post-2 Ma acceleration of exhumation affecting the study area at a larger scale. The observed acceleration is likely related to the Quaternary glaciations, which affected the entire Alpine orogen (Ehlers et al., 2011). As elaborated by previous studies, post-glacial isostatic adjustment (Champagnac et al., 2007; Persaud & Pfiffner, 2004) and enhanced glacial erosion (Fox et al., 2015; Valla et al., 2012) could produce very similar exhumation and uplift patterns. One of the key parameters defining the rate of glacial erosion is the ice sliding velocity (Herman et al., 2015). Models of the ice dynamics during the last glacial maximum in the Alps (Seguinot et al., 2018) highlight a band with ice sliding velocities higher than 300 m/a following the Rhine valley, which could have contributed to higher erosion rates in the easternmost Aar Massif. The impact of glacial erosion could be even more pronounced due to the presence of easily erodible Flysch and Bündnerschiefer units along the large and partly orogen-parallel Rhine catchment (Glaus et al., 2019; Schlunegger & Hinderer, 2001).

5.3. Potential Geodynamic Framework

As illustrated on Figure 12a, inherited lateral variations in the thickness and/or density could result in a different timing of basement-involved crustal thickening and exhumation in the underthrust lower plate of the orogen. In such a scenario, basement-involved deformation would first initiate in areas with a thicker and more buoyant crust as indicated by the red arrows on Figure 12a. Indications for inherited thickness variations can be found in the sedimentary cover of the Aar Massif. Mostly south-vergent normal faults separated the basement blocks of the Aar Massif and the Gotthard nappe already during the passive margin evolution (e.g., Trümpy et al., 1980). The Aar Massif, situated in the northern footwall block to these normal faults, was uplifted and exposed, as indicated by the absence of Early Jurassic sediments (i.e., “Allemannisches Land,” Pfiffner, 2015). Additionally, the Central Aare Granite, situated in the axial zone of the Aar Massif, represents one of the largest exposed intrusive bodies of the Alps (e.g., Berger, Mercolli, et al., 2017). On average, the density of this granite may be lower relative to the surrounding polycyclic metamorphic basement with an overall higher content in heavier mafic minerals. Both of these factors might have contributed to the early onset of basement-involved deformation in the central Aar Massif.

Additionally, along-strike changes in the thickness of syn-orogenic sediment deposits could cause a variable timing and magnitude of basement-involved deformation (Figure 12c, Erdős et al., 2015; Schwartz et al., 2017). According to these authors, a larger syn-orogenic sediment thickness favors thin-skinned tectonics and, thereby, delays the transition to basement-involved deformation. A corresponding increase in thickness of syn-orogenic Tertiary sediments, estimated based on the accreted cross sectional sediment thickness in Figure 5 from <3 km (transect B-B') to >6 km (transect D-D') would be consistent with an early initiation of thick-skinned deformation in the central Aar Massif. There might be a direct link between the thickness and density of the accreted crust as shown on Figure 12a and the geometry of the foreland basin.

Geophysical, geomorphological and isostatic considerations suggest that the tectonic evolution of the Central and Western Alps is strongly influenced by the dynamics of the European continental slab (see Kissling & Schlunegger, 2018, for a review). Two main aspects have to be considered with respect to the evolution of the Aar Massif. (a) It was recently proposed that delamination of mid to lower crustal material due to a rollback mechanism and the associated accretion of buoyant crustal material could drive vertical tectonic movements and explain the pattern of steep to sub-vertical reverse faults and rapid exhumation focused at the Aar Massif (Herwegh et al., 2017). (b) Seismic tomography reveals that the European continental slab appears to be detached below the Western Alps (Lippitsch et al., 2003), while a continuous slab is observable below the Central Alps. This was interpreted to reflect a lateral slab tear propagating to the

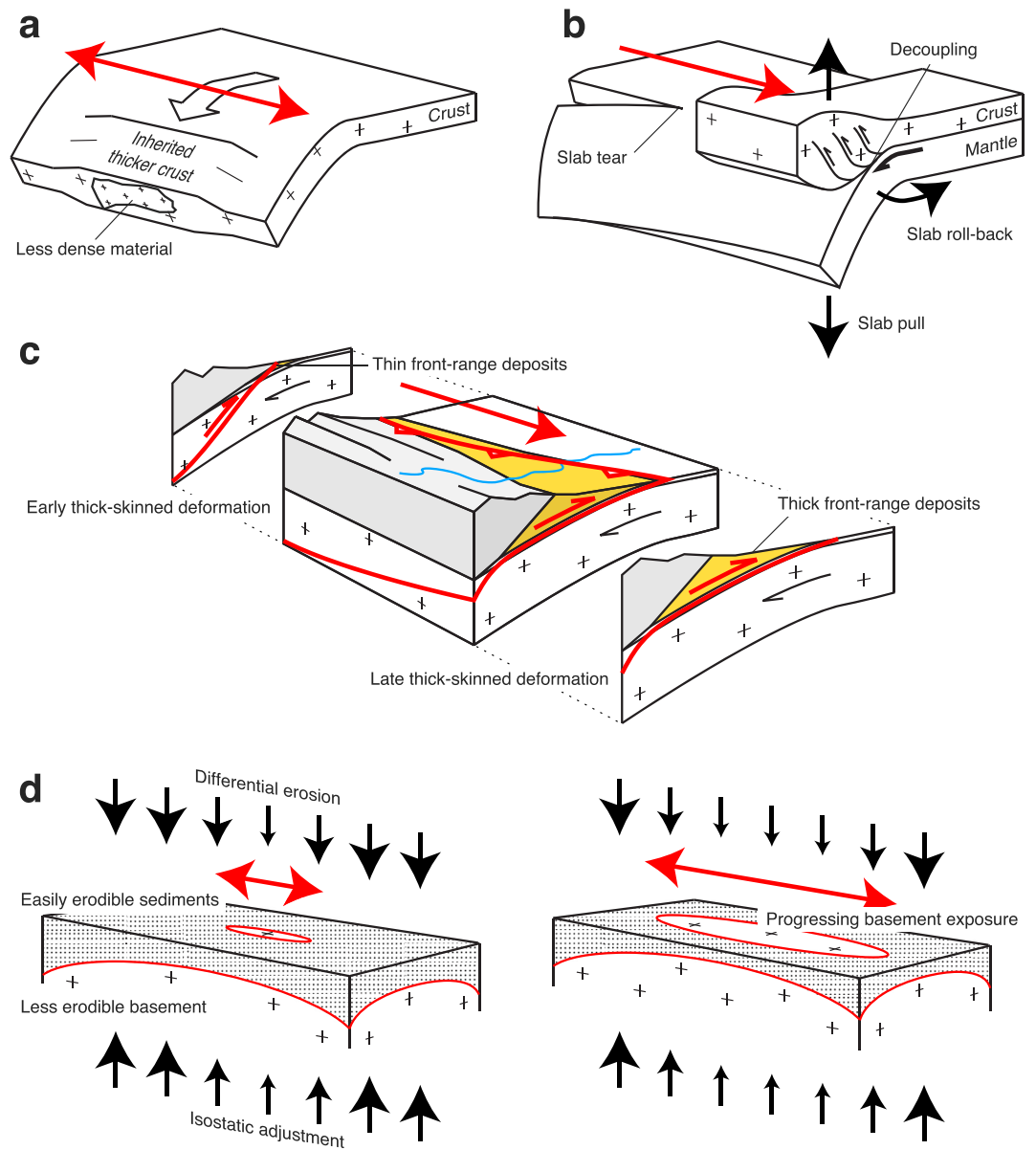


Figure 12. Schematic sketches of possible explanations for orogen-parallel migration of exhumation with time (red arrows): (a) shortening of a convex edge-shaped continental margin, (b) along-strike variations in the configuration of the continental slab or slab break-off and tear, propagating in orogen-parallel direction, (c) different timing of thick-skinned deformation due to thickness variation in the syn-orogenic front-range sediments, and (d) decrease of exhumation rates in the center of a dome due to the progressing exposure of less erodible basement units and isostatic adjustment.

northeast (Lippitsch et al., 2003). In the absence of detectable present-day convergence in the Western Alps (Nocquet et al., 2016), active slab detachment together with enhanced glacial erosion has been proposed to be responsible for the post-2 Ma increase in exhumation rates which is restricted to the Western Alps (Fox et al., 2015, 2016). Ongoing eastward propagation of the slab-detachment could potentially explain the migration of exhumation in eastward direction. However, the role of continental slab dynamics needs further geophysical investigations.

As discussed above, climate-driven erosion is considered to be one of the main driving forces for the Pliocene-Pleistocene increase of exhumation rates at the scale of the Western and Central Alps, and particularly

in the External Crystalline Massifs (e.g., Cederbom et al., 2004; Fox et al., 2015; Kuhlemann et al., 2002; Valla et al., 2012; Willett, 2010; Willett et al., 2006). Given the low plate convergence rates (2 mm/yr) estimated for the Neogene (Handy et al., 2010), efficient erosion is likely to play an important role also for the long-term exhumation history of the Aar Massif (Nibourel et al., 2018). However, changes in the climate cannot explain a lateral shift of peak exhumation rates at the scale of a 100 km over a time span of 10 Myr, such as the along-strike migration of peak exhumation in the eastern Aar Massif.

East of the Vättis window, the extent of maximum post-4 Ma exhumation shown on Figure 6 coincides with the exposure of easily erodible Flysch and Bündnerschiefer units (Schmid et al., 2004) rather than with the Aar Massif basement high (see top basement topography on Figure 1a). East of the Rhine Valley, these units are more than 6 km thick (Weh, 1998; Zerklaith et al., 2014). In our reconstruction (Figures 7b and 7c), the initiation of the eastward migration of exhumation coincides with the estimated first exposure of the crystalline basement in the central Aar Massif. As sketched on Figure 12d (left), the exposure of less erodible basement units, the associated decrease of erosion rates and isostasy-driven rock uplift could have led to lower exhumation rates in the central Aar Massif from 10 Ma onwards (Figure 7b). The progressing exposure of less erodible basement units with time could be a potential driver for the eastward migration of exhumation and for the rapid post-2 Ma exhumation of the Vättis area, also in the absence of significant convergence and crustal thickening (see Figure 12d, right). This scenario implies that the structural dome shape of the Aar Massif was most pronounced prior to its exposure at the surface approximately 10 Ma ago (Figure 11). According to Sternai et al. (2019), the isostatic adjustment due to deglaciation and erosion together account for 50% or more of the recent surface vertical displacements of the Central to Eastern Alps.

5.4. Implications for the Alps and Other Orogens

Our findings have important implications for Alpine tectonics, as they suggest that crustal thickening and associated differential exhumation, although at relatively slow rates and likely accelerated by the impact of the Pleistocene glaciation and by the exposure of easily erodible rocks at the surface, might still be active, especially at the eastern end of the Aar Massif. Comparable observations and interpretations were made by Schwartz et al. (2017) who found evidence for the exhumation of an incipient “hidden” External Crystalline Massif at a frontal position between the Pelvoux and Argentera massifs (Western Alps), which is clearly younger than the two adjacent exposed massifs.

Many studies have invoked a kinematic link between the Aar Massif and the Subalpine Molasse as well as the Jura fold-and-thrust belt (e.g., Boyer & Elliott, 1982; Burkhard, 1990; Burkhard & Sommaruga, 1998; Pfiffner, 1990; Pfiffner et al., 1997; von Hagke et al., 2012). In this regard, the diachronous exhumation pattern of the Aar Massif has implications for the prediction of long- and short-term dynamics, including seismic hazard, of the North Alpine Foreland. Other studies have also found evidence for slow but active and potentially basement-involved compressional deformation, for example in the Subalpine Molasse (Mock & Herwegh, 2017; von Hagke et al., 2014), in the Swiss Molasse basin (e.g., Ibele, 2011; Mock & Herwegh, 2017) and in the Jura mountains (Madritsch et al., 2010). An along-strike decrease of cooling ages in the Subalpine Molasse reflecting the cooling age and exhumation pattern of the Aar Massif is not observed (Heuberger et al., 2016; Mock et al., 2020; von Hagke et al., 2012, 2014). Instead, the youngest reset AFT and AHe ages from the Subalpine Molasse show relatively little lateral variation (e.g., Mock et al., 2020; Rahn, 2001), which questions the concept of a direct kinematic link between the External Crystalline Massifs and foreland deformation (see also von Hagke et al., 2014).

Noncylindrical massif growth may also affect other Alpine massifs and orogens, in which plates with inherited lateral irregularities are involved. Orogen-parallel migration of peak exhumation can explain both (a) the different timing of exhumation pulses at different localities along the External Crystalline Massifs (e.g., Glotzbach et al., 2010; Glotzbach, van der Beek, & Spiegel, 2011; Reinecker et al., 2008; van der Beek et al., 2010; Vernon et al., 2008; Vernon, van der Beek, Sinclair, Persano, et al., 2009) and (b) near steady-state exhumation rates but changing source areas at the scale of the Central and Western Alps as revealed by detrital thermochronometry (e.g., Bernet et al., 2001; Glotzbach, Bernet, & van der Beek, 2011). Because thermochronometric studies are commonly focused along orogen-perpendicular transects and located near

the center of structural domes, along-strike variations and exhumation dynamics have the potential to be overlooked.

6. Conclusions

The enhanced spatial resolution of new and published thermochronometric data together with estimates on metamorphic peak temperature offer the opportunity to quantitatively assess the Neogene exhumation history of the eastern Aar Massif in the directions perpendicular and parallel to the Alpine orogen. Our results highlight that maximum exhumation at rates of 1 mm/yr and more were focused on the central massif during an early stage between 22 and 10 Ma. The region with maximum exhumation rates then gradually migrated along-strike from the central to the eastern Aar Massif, while the central Aar Massif continued to exhume at slower rates (0.5 mm/yr). This indicates a noncylindrical evolution associated with eastward migration of exhumation in an orogen-parallel direction (i.e., perpendicular to the main orogenic transport direction).

In the central Aar Massif, exhumation dynamics are in good agreement with independent age and kinematic constraints from exposed fault zones. This suggests a strong link between exhumation and crustal-scale tectonic processes. Its noncylindrical exhumation points to crustal thickening as the main driving force for long-term exhumation, rather than climate change.

We infer that the noncylindrical evolution of the massif, including the migration of peak exhumation in orogen-parallel direction, mainly reflect variations in the timing of basement-involved deformation, associated crustal thickening and efficient erosion. The early initiation of basement-involved deformation in the central Aar Massif, relative to surrounding areas, may be due to a larger inherited thickness and/or a lower density of the crust. The decrease of exhumation rates in the central Aar Massif and the lateral migration of maximum exhumation rates in eastward direction from 10 Ma onwards may be enhanced by the progressing exposure of less erodible basement units in the central Aar Massif and by the presence of more easily erodible flysch and Bündnerschiefer units in the east of the study area.

The two-fold increase in exhumation rate between 2 Ma and present affecting the study area at a larger scale is attributed to enhanced erosion and isostatic adjustment due to glaciation/deglaciation since the Pleistocene. The good correlation between the post-2 Ma exhumation maximum and the top basement high of the eastern Aar Massif points to ongoing crustal thickening and thus the continuation of eastward migration of the Aar Massif growth to the present-day. This is supported by a similar distribution and magnitude of geodesy-based modern uplift rates and by earthquake focal-mechanisms indicating an increased tendency to thrust tectonics at the external front of the eastern Aar Massif.

Our findings suggest that crustal thickening, although at relatively slow rates and likely accelerated by the impact of the Pleistocene glaciation, might still be active, especially at the lateral edges of the External Crystalline Massifs and the adjacent forelands. Noncylindrical massif growth provides an explanation for the apparent mismatch between Alpine-wide steady-state exhumation, as suggested by detrital thermochronometry, and distinct exhumation peaks occurring at a variety of times, as revealed by regional-scale in situ thermochronometric studies. The process is likely to affect other Alpine massifs and mountain belts, but might be overlooked when studies focus on single orogen-perpendicular transects.

Data Availability Statement

All data included in the inverse model have been previously published (Berger et al., 2020; Campani et al., 2010; Cederbom et al., 2004; Ciancaleoni, 2005; Elfert et al., 2013; Evans, 2011; Giger, 1991; Glotzbach et al., 2009, 2010; Hess, 2003; Hunziker et al., 1992; Hurford, 1986; Janots et al., 2008; Keller et al., 2005; Lihou et al., 1995; Michalski & Soom, 1990; Mock et al., 2020; Price et al., 2018; Rahn, 1994, 2001; Rahn et al., 1997; Reinecker et al., 2008; Schaer et al., 1975; Spiegel et al., 2000, 2001; Steiner, 1984; Timar-Geng et al., 2004; Valla et al., 2016; Vernon, van der Beek, Sinclair, Persano, et al., 2009; von Hagke et al., 2012, 2014; Wagner et al., 1977, 1979; Wagner & Reimer, 1972; Weh, 1998; Weisenberger et al., 2012) or are available in Fox et al. (2015) which was the basis of the compilation used in this study. All new thermochronometric ages

from this study are listed in the Supporting Information S1. Samples and mineral separates are archived at the collection of the Institute of Geological Sciences (University of Bern).

Acknowledgments

The authors thank E. Kissling (ETH Zurich), D. Egli, S. Mock, and P. Valla (University of Bern) for fruitful discussions; D. Buess and A. Maltese (University of Bern) for help during mineral separation. M. G. Fellin (ETH Zurich) and J. Dunkl (University of Göttingen) helped selecting zircons. M. Fox (University College London) provided a compilation of thermochronometry data. M. A. Riedi, A. Brunner, M. Soland, A. Persson, and M. Peters are thanked for their help in the field. The authors thank D. Letsch for providing sample material. Hartsteinwerk Gasperini AG provided sample material from their quarry. The study was funded by the Swiss National Science Foundation project number 169055. Open access funding provided by University of Bern.

References

- Arnost, D. R. (2016). *Impact of meteoric fluid flow on the thermal evolution of Alpine exhumation: Insights from the Gotthard Base Tunnel, Switzerland* (PhD thesis, unpublished). University of Texas.
- Baumberger, R. (2015). *Quantification of lineaments: Link between internal 3D structure and surface evolution of the Hasli valley (Aar Massif, Central Alps, Switzerland)* (PhD thesis, unpublished). Universität Bern.
- Becker, A. (2000). The Jura Mountains—An active foreland fold-and-thrust belt? *Tectonophysics*, 321(4), 381–406. [https://doi.org/10.1016/S0040-1951\(00\)00089-5](https://doi.org/10.1016/S0040-1951(00)00089-5)
- Belgrano, T. M., Herwegh, M., & Berger, A. (2016). Inherited structural controls on fault geometry, architecture and hydrothermal activity: An example from Grimsel Pass, Switzerland. *Swiss Journal of Geosciences*, 109(3), 345–364. <https://doi.org/10.1007/s00015-016-0212-9>
- Bellahsen, N., Mouthereau, F., Boutoux, A., Bellanger, M., Lacombe, O., Jolivet, L., & Rolland, Y. (2014). Collision kinematics in the western external Alps. *Tectonics*, 33(6), 1055–1088. <https://doi.org/10.1002/2013TC003453>
- Bergmann, C., Gnos, E., Berger, A., Whitehouse, M., Mullis, J., Wehrens, P., et al. (2017). Th-Pb ion probe dating of zoned hydrothermal monazite and its implications for repeated shear zone activity: An example from the Central Alps, Switzerland. *Tectonics*, 36(4), 671–689. <https://doi.org/10.1002/2016TC004407>
- Berger, A., Engi, M., Erne-Schmid, S., Glotzbach, C., Spiegel, C., de Goede, R., & Herwegh, M. (2020). The relation between peak metamorphic temperatures and subsequent cooling during continent–continent collision (western Central Alps, Switzerland). *Swiss Journal of Geosciences*, 113(1), 1–18. <https://doi.org/10.1186/s00015-020-00356-4>
- Berger, A., Mercolli, I., Herwegh, M., & Gnos, E. (2017). *Geological map of the Aar Massif, Tavetsch and Gotthard Nappes* (Geological Special Map 129, Explanatory notes).
- Berger, A., Wehrens, P., Lanari, P., Zwingmann, H., & Herwegh, M. (2017). Microstructures, mineral chemistry and geochronology of white micas along a retrograde evolution: An example from the Aar massif (Central Alps, Switzerland). *Tectonophysics*, 721, 179–195. <https://doi.org/10.1016/j.tecto.2017.09.019>
- Bernet, M., Brandon, M. T., Garver, J. I., Balestrieri, M., Ventura, B., & Zattin, M. (2009). Exhuming the Alps through time: Clues from detrital zircon fission-track thermochronology. *Basin Research*, 21(6), 781–798. <https://doi.org/10.1111/j.1365-2117.2009.00400.x>
- Bernet, M., Brandon, M. T., Garver, J. I., & Molitor, B. R. (2004). *Fundamentals of detrital zircon fission-track analysis for provenance and exhumation studies with examples from the European Alps* (pp. 25–36). Special Papers—Geological Society of America. <https://doi.org/10.1130/0-8137-2378-7.25>
- Bernet, M., & Spiegel, C. (2004). Detrital thermochronology: Provenance analysis, exhumation, and landscape evolution of mountain belts (Vol. 378). Geological Society of America.
- Bernet, M., Zattin, M., Garver, J. I., Brandon, M. T., & Vance, J. A. (2001). Steady-state exhumation of the European Alps. *Geology*, 29(1), 35–38. [https://doi.org/10.1130/0091-7613\(2001\)029<0035:seote>2.0.co;2](https://doi.org/10.1130/0091-7613(2001)029<0035:seote>2.0.co;2)
- Beysnac, O., Goffé, B., Chopin, C., & Rouzaud, J. (2002). Raman spectra of carbonaceous material in metasediments: A new geothermometer. *Journal of Metamorphic Geology*, 20(9), 859–871. <https://doi.org/10.1046/j.1525-1314.2002.00408.x>
- Bodmer, P., & Rybach, L. (1984). Geothermal map of Switzerland (heat flow density). In *Beiträge zur Geologie der Schweiz: Geophysik* (p. 22).
- Boutoux, A., Bellahsen, N., Nanni, U., Pik, R., Verlaquet, A., Rolland, Y., & Lacombe, O. (2016). Thermal and structural evolution of the external Western Alps: Insights from (U–Th–Sm)/He thermochronology and rsm thermometry in the Aiguilles Rouges/Mont Blanc Massifs. *Tectonophysics*, 683, 109–123. <https://doi.org/10.1016/j.tecto.2016.06.010>
- Boyer, S. E., & Elliott, D. (1982). Thrust systems. *AAPG Bulletin*, 66(9), 1196–1230. <https://doi.org/10.1306/03b5a77d-16d1-11d7-8645000102c1865d>
- Brandon, M. T., Roden-Tice, M. K., & Garver, J. I. (1998). Late Cenozoic exhumation of the Cascadia accretionary wedge in the Olympic Mountains, northwest Washington State. *Geological Society of America Bulletin*, 110(8), 985–1009. [https://doi.org/10.1130/0016-7606\(1998\)110<0985:lceotc>2.3.co;2](https://doi.org/10.1130/0016-7606(1998)110<0985:lceotc>2.3.co;2)
- Brückner, W., & Zbinden, P. (1987). *Atlasblatt 1192 Schächental, 1:25 000*. Geologischer Atlas der Schweiz, swisstopo, Erläuterungen 83.
- Burkhard, M. (1988). L'Helvétique de la bordure occidentale du massif de l'Aar (évolution tectonique et métamorphique). *Eclogae Geologicae Helveticae*, 81(1), 63–114. <https://doi.org/10.5169/seals-166171>
- Burkhard, M. (1990). Aspects of the large-scale Miocene deformation in the most external part of the Swiss Alps (Subalpine Molasse to Jura fold belt). *Eclogae Geologicae Helveticae*, 83(3), 559–583. <https://doi.org/10.5169/seals-166602>
- Burkhard, M., & Sommaruga, A. (1998). Evolution of the western Swiss Molasse basin: Structural relations with the Alps and the Jura belt. *Geological Society, London, Special Publications*, 134(1), 279–298. <https://doi.org/10.1144/GSL.SP.1998.134.01.13>
- Burtner, R. L., Nigrini, A., & Donelick, R. A. (1994). Thermochronology of lower cretaceous source rocks in the idaho-wyoming thrust belt. *AAPG Bulletin*, 78(10), 1613–1636. <https://doi.org/10.1306/a25ff233-171b-11d7-8645000102c1865d>
- Campani, M., Mancktelow, N., Seward, D., Rolland, Y., Müller, W., & Guerra, I. (2010). Geochronological evidence for continuous exhumation through the ductile–brittle transition along a crustal-scale low-angle normal fault: Simplon Fault Zone, central Alps. *Tectonics*, 29(3). <https://doi.org/10.1029/2009TC002582>
- Campani, M., Mulch, A., Kempf, O., Schlunegger, F., & Mancktelow, N. (2012). Miocene paleotopography of the Central Alps. *Earth and Planetary Science Letters*, 337–338, 174–185. <https://doi.org/10.1016/j.epsl.2012.05.017>
- Cederbom, C. E., Sinclair, H. D., Schlunegger, F., & Rahn, M. K. (2004). Climate-induced rebound and exhumation of the European Alps. *Geology*, 32(8), 709–712. <https://doi.org/10.1130/g20491.1>
- Cederbom, C. E., van der Beek, P., Schlunegger, F., Sinclair, H. D., & Oncken, O. (2011). Rapid extensive erosion of the North Alpine foreland basin at 5–4 Ma. *Basin Research*, 23(5), 528–550. <https://doi.org/10.1111/j.1365-2117.2011.00501.x>
- Challandes, N., Marquer, D., & Villa, I. M. (2008). PT modelling, fluid circulation, and 39 Ar–40 Ar and Rb–Sr mica ages in the Aar Massif shear zones (Swiss Alps). *Swiss Journal of Geosciences*, 101(2), 269–288. <https://doi.org/10.1007/s00015-008-1260-6>
- Champagnac, J.-D., Molnar, P., Anderson, R., Sue, C., & Delacou, B. (2007). Quaternary erosion-induced isostatic rebound in the Western Alps. *Geology*, 35(3), 195–198. <https://doi.org/10.1130/G23053A.1>
- Choukroune, P., & Gapais, D. (1983). Strain pattern in the Aar granite (Central Alps): Orthogneiss developed by bulk inhomogeneous flattening. In *Strain patterns in rocks* (pp. 411–418). Elsevier. <https://doi.org/10.1016/B978-0-08-030273-7.50019-7>

- Ciancaleoni, L. (2005). *Deformation processes during the last stages of the continental collision* (PhD thesis, unpublished). Université de Neuchâtel.
- Crowley, K., Cameron, M., & Schaefer, R. (1991). Experimental studies of annealing of etched fission tracks in fluorapatite. *Geochimica et Cosmochimica Acta*, 55(5), 1449–1465. [https://doi.org/10.1016/0016-7037\(91\)90320-5](https://doi.org/10.1016/0016-7037(91)90320-5)
- Deichmann, N. (2014). *Earthquakes in Switzerland and surrounding regions 1996–2012, version 2014.1* (Technical report). Swiss Seismological Service, ETH Zürich.
- Deichmann, N., Baer, M., Braunmiller, J., Dolfin, D. B., Bay, F., Delouis, B., & Wiemer, S. (2000). Earthquakes in Switzerland and surrounding region during 1999. *Eclogae Geologicae Helveticae*, 93(3), 395–406.
- Diehl, T., Clinton, J., Deichmann, N., Cauzzi, C., Kästli, P., Kraft, T., et al. (2018). Earthquakes in Switzerland and surrounding regions during 2015 and 2016. *Swiss Journal of Geosciences*, 111(1–2), 221–244. <https://doi.org/10.1007/s00015-017-0295-y>
- Diehl, T., Clinton, J., Kraft, T., Husen, S., Plenkers, K., Guilhem, A., et al. (2014). Earthquakes in Switzerland and surrounding regions during 2013. *Swiss Journal of Geosciences*, 107(2–3), 359–375. <https://doi.org/10.1007/s00015-014-0171-y>
- Diehl, T., Deichmann, N., Clinton, J., Kästli, P., Cauzzi, C., Kraft, T., et al. (2015). Earthquakes in Switzerland and surrounding regions during 2014. *Swiss Journal of Geosciences*, 106(1515), 543–443. <https://doi.org/10.1007/s00015-015-0204-1>
- Diefendorfer, A. (2017). Constraining the strength of megathrusts from fault geometries and application to the Alpine collision zone. *Earth and Planetary Science Letters*, 474, 49–58. <https://doi.org/10.1016/j.epsl.2017.06.021>
- Diefendorfer, A., Berger, A., & Herwegh, M. (2016). The accretion of foreland basin sediments during early stages of continental collision in the European Alps and similarities to accretionary wedge tectonics. *Tectonics*, 35(10), 2216–2238. <https://doi.org/10.1002/2015TC004101>
- Dixon, W. J. (1950). Analysis of extreme values. *The Annals of Mathematical Statistics*, 21(4), 488–506. <https://doi.org/10.1214/aoms/1177729747>
- Dodson, M. H. (1973). Closure temperature in cooling geochronological and petrological systems. *Contributions to Mineralogy and Petrology*, 40(3), 259–274. <https://doi.org/10.1007/BF00373790>
- Donelick, R. A., Ketchum, R. A., & Carlson, W. D. (1999). Variability of apatite fission-track annealing kinetics II: Crystallographic orientation effects. *American Mineralogist*, 84(9), 1224–1234. <https://doi.org/10.2138/am-1999-0902>
- Donelick, R. A., O'Sullivan, P. B., & Ketchum, R. A. (2005). Apatite fission-track analysis. *Reviews in Mineralogy and Geochemistry*, 58(1), 49–94. <https://doi.org/10.2138/rmg.2005.58.3>
- Dunkl, I., Di Giulio, A., & Kuhlemann, J. (2001). Combination of single-grain fission-track chronology and morphological analysis of detrital zircon crystals in provenance studies: Sources of the Macigno Formation (Apennines, Italy). *Journal of Sedimentary Research*, 71(4), 516–525. <https://doi.org/10.1306/102900710516>
- Egli, D., Baumann, R., Küng, S., Berger, A., Baron, L., & Herwegh, M. (2018). Structural characteristics, bulk porosity and evolution of an exhumed long-lived hydrothermal system. *Tectonophysics*, 747, 239–258. <https://doi.org/10.1016/j.tecto.2018.10.008>
- Egli, D., & Mancktelow, N. (2013). The structural history of the Mont Blanc Massif with regard to models for its recent exhumation. *Swiss Journal of Geosciences*, 106(3), 469–489. <https://doi.org/10.1007/s00015-013-0153-5>
- Ehlers, J., Ehlers, J., Gibbard, P., & Hughes, P. (2011). *Quaternary glaciations—extent and chronology: A closer look* (Vol. 15). Elsevier. Retrieved from <https://booksite.elsevier.com/9780444534477/>
- Elfert, S., Reiter, W., & Spiegel, C. (2013). Long-lasting tectonic activities of the Lepontine Dome. New evidence from low-temperature thermochronology. *Tectonophysics*, 608, 222–236. <https://doi.org/10.1016/j.tecto.2013.09.033>
- Erdős, Z., Huismans, R. S., & Beek, P. (2015). First-order control of syntectonic sedimentation on crustal-scale structure of mountain belts. *Journal of Geophysical Research: Solid Earth*, 120(7), 5362–5377. <https://doi.org/10.1002/2014JB011785>
- Erne, S. (2014). *Temperaturabschätzung der Metasedimente zwischen Gotthard- und Aar-Massiv in der Urseren-Garvera Zone, mittels Raman-spektroskopie* (Bachelor thesis, unpublished). Universität Bern.
- Evans, S. L. (2011). *Timing of exhumation of the eastern Central Alps from zircon and apatite (U-Th)/He thermochronology (Graubünden, Switzerland)* (PhD thesis, unpublished). University of Kansas.
- Farley, K. A., Wolf, R., & Silver, L. (1996). The effects of long alpha-stopping distances on (U-Th)/He ages. *Geochimica et Cosmochimica Acta*, 60(21), 4223–4229. [https://doi.org/10.1016/S0016-7037\(96\)00193-7](https://doi.org/10.1016/S0016-7037(96)00193-7)
- Fox, M., Herman, F., Kissling, E., & Willett, S. D. (2015). Rapid exhumation in the Western Alps driven by slab detachment and glacial erosion. *Geology*, 43(5), 379–382. <https://doi.org/10.1130/G36411.1>
- Fox, M., Herman, F., Willett, S., & May, D. (2014). A linear inversion method to infer exhumation rates in space and time from thermochronometric data. *Earth Surface Dynamics*, 2(1), 47–65. <https://doi.org/10.5194/esurf-2-47-2014>
- Fox, M., Herman, F., Willett, S. D., & Schmid, S. M. (2016). The exhumation history of the European Alps inferred from linear inversion of thermochronometric data. *American Journal of Science*, 316(6), 505–541. <https://doi.org/10.2475/06.2016.01>
- Frey, M., & Ferreiro-Mählmann, R. (1999). Alpine metamorphism of the Central Alps. *Schweizerische Mineralogische und Petrographische Mitteilungen*, 79(1), 135–154. <https://doi.org/10.3390/geosciences7030071>
- Froitzheim, N., Schmid, S. M., & Frey, M. (1996). Mesozoic paleogeography and the timing of eclogite-facies metamorphism in the Alps: A working hypothesis. *Eclogae Geologicae Helveticae*, 89(1), 81. <https://doi.org/10.5169/seals-167895>
- Fügensschuh, B., & Schmid, S. (2003). Late stages of deformation and exhumation of an orogen constrained by fission-track data: A case study in the Western Alps. *Geological Society of America Bulletin*, 115(11), 1425–1440. <https://doi.org/10.1130/B25092.1>
- Gallagher, K., Brown, R., & Johnson, C. (1998). Fission track analysis and its applications to geological problems. *Annual Review of Earth and Planetary Sciences*, 26(1), 519–572. <https://doi.org/10.1146/annurev.earth.26.1.519>
- Garver, J., Reiners, P., Walker, L. J., Ramage, J., & Perry, S. (2005). Implications for timing of Andean uplift from thermal resetting of radiation-damaged zircon in the Cordillera Huayhuash, northern Peru. *The Journal of Geology*, 113(2), 117–138. <https://doi.org/10.1086/427664>
- Gasser, D., & Den Brok, B. (2008). Tectonic evolution of the Engi slates, Glarus Alps, Switzerland. *Swiss Journal of Geosciences*, 101(2), 311–322. <https://doi.org/10.1007/s00015-008-1258-0>
- Giger, M. (1991). *Geochronologische und petrographische Studien an Geröll und Sedimenten der Gonfolite Lombarda Gruppe (Südschweiz und Norditalien) und ihr Vergleich mit dem alpinen Hinterland* (PhD thesis, unpublished). Universität Bern.
- Girault, J., Bellahsen, N., Boutoux, A., Rosenberg, C., Nanni, U., Verlaquet, A., & Beyssac, O. (2020). The 3-D thermal structure of the Helvetic nappes of the European Alps: Implications for collisional processes. *Tectonics*, 39(3), e2018TC005334. <https://doi.org/10.1029/2018TC005334>
- Glaus, G., Delunel, R., Stutenbecker, L., Akçar, N., Christl, M., & Schlunegger, F. (2019). Differential erosion and sediment fluxes in the Landquart basin and possible relationships to lithology and tectonic controls. *Swiss Journal of Geosciences*, 112(2–3), 453–473. <https://doi.org/10.1007/s00015-019-00344-3>

- Glotzbach, C., Bernet, M., & van der Beek, P. (2011). Detrital thermochronology records changing source areas and steady exhumation in the Western European Alps. *Geology*, 39(3), 239–242. <https://doi.org/10.1130/G31757.1>
- Glotzbach, C., Reinecker, J., Danišik, M., Rahn, M. K., Frisch, W., & Spiegel, C. (2010). Thermal history of the central Gotthard and Aar Massifs, European Alps: Evidence for steady state, long-term exhumation. *Journal of Geophysical Research*, 115, F03017. <https://doi.org/10.1029/2009JF001304>
- Glotzbach, C., Spiegel, C., Reinecker, J., Rahn, M., & Frisch, W. (2009). What perturbs isotherms? An assessment using fission-track thermochronology and thermal modelling along the Gotthard transect, Central Alps. *Geological Society, London, Special Publications*, 324(1), 111–124. <https://doi.org/10.1144/SP324.9>
- Glotzbach, C., van der Beek, P. A., & Spiegel, C. (2011). Episodic exhumation and relief growth in the Mont Blanc Massif, Western Alps from numerical modelling of thermochronology data. *Earth and Planetary Science Letters*, 304(3–4), 417–430. <https://doi.org/10.1016/j.epsl.2011.02.020>
- Goncalves, P., Oliot, E., Marquer, D., & Connolly, J. (2012). Role of chemical processes on shear zone formation: An example from the grimsel metagranodiorite (Aar Massif, Central Alps). *Journal of Metamorphic Geology*, 30(7), 703–722. <https://doi.org/10.1111/j.1525-1314.2012.00991.x>
- Green, P., Duddy, I., Gleadow, A. J. W., Tingate, P., & Laslett, G. (1986). Thermal annealing of fission tracks in apatite. *Chemical Geology: Isotope Geoscience Section*, 59, 237–253. [https://doi.org/10.1016/0168-9622\(86\)90074-6](https://doi.org/10.1016/0168-9622(86)90074-6)
- Grubbs, F. E. (1950). Sample criteria for testing outlying observations. *The Annals of Mathematical Statistics*, 21, 27–58. <https://doi.org/10.1214/aoms/1177729885>
- Guenther, W. R., Reiners, P. W., Ketcham, R. A., Nasdala, L., & Giester, G. (2013). Helium diffusion in natural zircon: Radiation damage, anisotropy, and the interpretation of zircon (u-th)/he thermochronology. *American Journal of Science*, 313(3), 145–198. <https://doi.org/10.2475/03.2013.01>
- Hafner, S. (2016). *The thermal peak in metamorphic black shales: Gradients in the Valaisan units and contrast to tectonic neighbors* (Master thesis, unpublished). Universität Bern.
- Handy, M. R., Schmid, S. M., Bousquet, R., Kissling, E., & Bernoulli, D. (2010). Reconciling plate-tectonic reconstructions of Alpine Tethys with the geological–geophysical record of spreading and subduction in the Alps. *Earth-Science Reviews*, 102(3–4), 121–158. <https://doi.org/10.1016/j.earscirev.2010.06.002>
- Herman, F., Beyssac, O., Brughelli, M., Lane, S. N., Leprince, S., Adatte, T., et al. (2015). Erosion by an alpine glacier. *Science*, 350(6257), 193–195. <https://doi.org/10.1126/science.aab2386>
- Herman, F., & Brandon, M. (2015). Mid-latitude glacial erosion hotspot related to equatorial shifts in southern Westerlies. *Geology*, 43(11), 987–990. <https://doi.org/10.1130/G37008.1>
- Herwegh, M., Berger, A., Baumberger, R., Wehrens, P., & Kissling, E. (2017). Large-scale crustal-block-extrusion during late Alpine collision. *Scientific Reports*, 7, 413. <https://doi.org/10.1038/s41598-017-00440-0>
- Herwegh, M., Berger, A., Bellahsen, N., Rolland, Y., & Kissling, E. (in press). Evolution of the External Crystalline Massifs of the European Alps: From Massif to Lithosphere Scale. Evolution of the External Crystalline Massifs of the European Alps: From Massif to Lithosphere Scale. In C. Rosenberg, & N. Bellahsen (Eds.), *Geodynamics of the Alps*.
- Herwegh, M., Berger, A., Glotzbach, C., Wangenheim, C., Mock, S., Wehrens, P., et al. (2020). Late stages of continent-continent collision: Timing, kinematic evolution, and exhumation of the Northern rim (Aar Massif) of the Alps. *Earth-Science Reviews*, 200, 102959. <https://doi.org/10.1016/j.earscirev.2019.102959>
- Herwegh, M., Hürzeler, J.-P., Pfiffner, O. A., Schmid, S. M., Abart, R., & Ebert, A. (2008). The Glarus thrust: Excursion guide and report of a field trip of the Swiss Tectonic Studies Group (Swiss Geological Society, 14.–16. 09. 2006). *Swiss Journal of Geosciences*, 101(2), 323–340. <https://doi.org/10.1007/s00015-008-1259-z>
- Herwegh, M., & Pfiffner, O. A. (2005). Tectono-metamorphic evolution of a nappe stack: A case study of the Swiss Alps. *Tectonophysics*, 404(1–2), 55–76. <https://doi.org/10.1016/j.tecto.2005.05.002>
- Hess, M. (2003). *Strukturgeologie und Spaltspurdatierungen an Apatit und Zirkon an der Simplonlinie im Gebiet um Domodossola (I)* (PhD thesis, unpublished). Universität Basel.
- Heuberger, S., Roth, P., Zingg, O., Naef, H., & Meier, B. P. (2016). The St. Gallen Fault Zone: A long-lived, multiphase structure in the North Alpine Foreland Basin revealed by 3D seismic data. *Swiss Journal of Geosciences*, 109(1), 83–102. <https://doi.org/10.1007/s00015-016-0208-5>
- Hitz, L., & Pfiffner, O.-A. (1994). A 3D crustal model of the Eastern External Aar Massif interpreted from a network of deep seismic profiles. *Schweizerische Mineralogische und Petrographische Mitteilungen*, 74, 405–420. <https://doi.org/10.5169/seals-56356>
- Hourigan, J. K., Reiners, P. W., & Brandon, M. T. (2005). U-Th zonation-dependent alpha-ejection in (U-Th)/He chronometry. *Geochimica et Cosmochimica Acta*, 69(13), 3349–3365. <https://doi.org/10.1016/j.gca.2005.01.024>
- Hunziker, J. C., Desmons, J., & Hurford, A. J. (1992). *Thirty-two years of geochronological work in the Central and Western Alps: A review on seven maps*. Mémoires de Géologie 13. [https://doi.org/10.1016/8756-3282\(92\)90369-8](https://doi.org/10.1016/8756-3282(92)90369-8)
- Hunziker, J. C., Frey, M., Clauer, N., Dallmeyer, R., Friedrichsen, H., Flehmig, W., et al. (1986). The evolution of illite to muscovite: Mineralogical and isotopic data from the Glarus Alps, Switzerland. *Contributions to Mineralogy and Petrology*, 92(2), 157–180. <https://doi.org/10.1007/BF00375291>
- Hurford, A. J. (1986). Cooling and uplift patterns in the Lepontine Alps South Central Switzerland and an age of vertical movement on the Insubric fault line. *Contributions to Mineralogy and Petrology*, 92(4), 413–427. <https://doi.org/10.1007/BF00374424>
- Hurford, A. J. (1990). Standardization of fission track dating calibration: Recommendation by the fission track working group of the iugs subcommission on geochronology. *Chemical Geology: Isotope Geoscience Section*, 80(2), 171–178. [https://doi.org/10.1016/0168-9622\(90\)90025-8](https://doi.org/10.1016/0168-9622(90)90025-8)
- Hurford, A. J., & Green, P. F. (1982). A users' guide to fission track dating calibration. *Earth and Planetary Science Letters*, 59(2), 343–354. [https://doi.org/10.1016/0012-821X\(82\)90136-4](https://doi.org/10.1016/0012-821X(82)90136-4)
- Ibele, T. (2011). *Tectonics of the western Swiss Molasse Basin during Cenozoic times* (PhD thesis, unpublished). University of Fribourg.
- Janots, E., Berger, A., Gnos, E., Whitehouse, M., Lewin, E., & Pettke, T. (2012). Constraints on fluid evolution during metamorphism from U–Th–Pb systematics in Alpine hydrothermal monazite. *Chemical Geology*, 326, 61–71. <https://doi.org/10.1016/j.chemgeo.2012.07.014>
- Janots, E., Engi, M., Berger, A., Allaz, J., Schwarz, J.-O., & Spandler, C. (2008). Prograde metamorphic sequence of REE minerals in pelitic rocks of the Central Alps: Implications for allanite–monazite–xenotime phase relations from 250 to 610 C. *Journal of Metamorphic Geology*, 26(5), 509–526. <https://doi.org/10.1111/j.1525-1314.2008.00774.x>
- Janots, E., & Rubatto, D. (2014). U–Th–Pb dating of collision in the external Alpine domains (Urseren zone, Switzerland) using low temperature allanite and monazite. *Lithos*, 184, 155–166. <https://doi.org/10.1016/j.lithos.2013.10.036>

- Jarvis, A., Reuter, H., Nelson, A., & Guevara, E. (2006). *Void-filled seamless SRTM data V3*. Retrieved from <http://srtm.csi.cgiar.org>
- Jiao, R., Herman, F., & Seward, D. (2017). Late Cenozoic exhumation model of New Zealand: Impacts from tectonics and climate. *Earth-Science Reviews*, *166*, 286–298. <https://doi.org/10.1016/j.earscirev.2017.01.003>
- Käch, P. (1972). *Geologie der Brigelserhörner: (Bündnerisches Vorderrheintal)* (Dissertation, unpublished). ETH Zürich.
- Kastrup, U., Zoback, M. L., Deichmann, N., Evans, K. F., Giardini, D., & Michael, A. J. (2004). Stress field variations in the Swiss Alps and the northern Alpine foreland derived from inversion of fault plane solutions. *Journal of Geophysical Research*, *109*, B01402. <https://doi.org/10.1029/2003JB002550>
- Kasuya, M., & Naeser, C. W. (1988). The effect of α -damage on fission-track annealing in zircon. *International Journal of Radiation Applications and Instrumentation. Part D. Nuclear Tracks and Radiation Measurements*, *14*(4), 477–480. [https://doi.org/10.1016/1359-0189\(88\)90008-8](https://doi.org/10.1016/1359-0189(88)90008-8)
- Keller, L. M., Hess, M., Fügenschuh, B., & Schmid, S. M. (2005). Structural and metamorphic evolution of the Camughera–Moncucco, Antrona and Monte Rosa units southwest of the Simplon line, Western Alps. *Eclogae Geologicae Helveticae*, *98*(1), 19–49. <https://doi.org/10.1007/s00015-005-1149-6>
- Kempf, O., Matter, A., Burbank, D. W., & Mange, M. (1999). Depositional and structural evolution of a foreland basin margin in a magnetostratigraphic framework: The eastern Swiss Molasse Basin. *International Journal of Earth Sciences*, *88*(2), 253–275. <https://doi.org/10.1007/s005310050263>
- Kissling, E., & Schlunegger, F. (2018). Rollback orogeny model for the evolution of the Swiss Alps. *Tectonics*, *37*(4), 1097–1115. <https://doi.org/10.1002/2017TC004762>
- Kuhlemann, J. (2000). Post-collisional sediment budget of circum-Alpine basins (Central Europe). *Memorie di Scienze Geologiche*, *52*(1), 1–91.
- Kuhlemann, J., Frisch, W., Székely, B., Dunkl, I., & Kázmér, M. (2002). Post-collisional sediment budget history of the Alps: Tectonic versus climatic control. *International Journal of Earth Sciences*, *91*(5), 818–837. <https://doi.org/10.1007/s00531-002-0266-y>
- Kuhlemann, J., & Kempf, O. (2002). Post-Eocene evolution of the North Alpine Foreland Basin and its response to Alpine tectonics. *Sedimentary Geology*, *152*(1–2), 45–78. [https://doi.org/10.1016/S0037-0738\(01\)00285-8](https://doi.org/10.1016/S0037-0738(01)00285-8)
- Lahfid, A., Beyssac, O., Deville, E., Negro, F., Chopin, C., & Goffé, B. (2010). Evolution of the Raman spectrum of carbonaceous material in low-grade metasediments of the Glarus Alps (Switzerland). *Terra Nova*, *22*(5), 354–360. <https://doi.org/10.1111/j.1365-3121.2010.00956.x>
- Lihou, J., Hurfurd, A., & Carter, A. (1995). Preliminary fission-track ages on zircons and apatites from the Sardona unit, Glarus Alps, eastern Switzerland: Late Miocene-Pliocene exhumation rates. *Schweizerische Mineralogische und Petrographische Mitteilungen*, *75*(2), 177–186. <https://doi.org/10.5169/seals-57149>
- Lippitsch, R., Kissling, E., & Ansorge, J. (2003). Upper mantle structure beneath the Alpine orogen from high-resolution teleseismic tomography. *Journal of Geophysical Research*, *108*(B8), 2376. <https://doi.org/10.1029/2002JB002016>
- Looser, N., Madritsch, H., Guillong, M., Laurent, O., Wohlwend, S., & Bernasconi, S. (2021). Absolute age and temperature constraints on deformation along the basal décollement of the Jura fold-and-thrust belt from carbonate U-Pb dating and clumped isotopes. *Tectonics*, *40*(3), e2020TC006439. <https://doi.org/10.1029/2020TC006439>
- Lu, G., Winkler, W., Rahn, M., Von Quadt, A., & Willett, S. D. (2018). Evaluating igneous sources of the Taveyannaz formation in the Central Alps by detrital zircon U–Pb age dating and geochemistry. *Swiss Journal of Geosciences*, *111*, 1–18. <https://doi.org/10.1007/s00015-018-0302-y>
- Madritsch, H., Preusser, F., Fabbri, O., Bichet, V., Schlunegger, F., & Schmid, S. M. (2010). Late Quaternary folding in the Jura Mountains: Evidence from syn-erosional deformation of fluvial meanders. *Terra Nova*, *22*(2), 147–154. <https://doi.org/10.1111/j.1365-3121.2010.00928.x>
- Mair, D., Lechmann, A., Herwegh, M., Nibourel, L., & Schlunegger, F. (2018). Linking Alpine deformation in the Aar Massif basement and its cover units—the case of the Jungfrau–Eiger Mountains (Central Alps, Switzerland). *Solid Earth*, *9*, 1099–1122. <https://doi.org/10.5194/se-9-1099-2018>
- Mancktelow, N. S., & Grasemann, B. (1997). Time-dependent effects of heat advection and topography on cooling histories during erosion. *Tectonophysics*, *270*(3–4), 167–195. [https://doi.org/10.1016/S0040-1951\(96\)00279-X](https://doi.org/10.1016/S0040-1951(96)00279-X)
- Marschall, I., Deichmann, N., & Marone, F. (2013). Earthquake focal mechanisms and stress orientations in the eastern Swiss Alps. *Swiss Journal of Geosciences*, *106*(1), 79–90. <https://doi.org/10.1007/s00015-013-0129-5>
- Menkveld-Gfeller, U., Kempf, O., & Funk, H. (2016). Lithostratigraphic units of the Helvetic Palaeogene: Review, new definition, new classification. *Swiss Journal of Geosciences*, *109*(2), 171–199. <https://doi.org/10.1007/s00015-016-0217-4>
- Michalski, I., & Soom, M. (1990). The Alpine thermo-tectonic evolution of the Aar and Gotthard massifs, Central Switzerland: Fission Track ages on zircon and apatite and K-Ar mica ages. *Schweizerische mineralogische und petrographische Mitteilungen*, *70*, 373–387. <https://doi.org/10.5169/seals-53628>
- Milnes, A. G., & Pfiffner, O.-A. (1977). Structural development of the Infrahelvetic complex, eastern Switzerland. *Eclogae Geologicae Helveticae*, *70*(1), 83–95. <https://doi.org/10.5169/seals-164615>
- Mock, S. (2014). *Deformation of the sediment-crystalline contact in the northern Aar Massif (Innertkirchen, Bernese Oberland)* (Master thesis, unpublished). Universität Bern.
- Mock, S., & Herwegh, M. (2017). Tectonics of the central Swiss Molasse Basin: Post-Miocene transition to incipient thick-skinned tectonics? *Tectonics*, *36*(9), 1699–1723. <https://doi.org/10.1002/2017TC004584>
- Mock, S., von Hagke, C., Schlunegger, F., Dunkl, I., & Herwegh, M. (2020). Long-wavelength late-Miocene thrusting in the north Alpine foreland: Implications for late orogenic processes. *Solid Earth*, *11*(5), 1823–1847. <https://doi.org/10.5194/se-11-1823-2020>
- Muñoz, J. A. (1992). Evolution of a continental collision belt: ECORS-Pyrenees crustal balanced cross-section. In *Thrust tectonics* (pp. 235–246). Springer. https://doi.org/10.1007/978-94-011-3066-010.1007/978-94-011-3066-0_21
- Nasdala, L., Reiners, P. W., Garver, J. I., Kennedy, A. K., Stern, R. A., Balan, E., & Wirth, R. (2004). Incomplete retention of radiation damage in zircon from Sri Lanka. *American Mineralogist*, *89*(1), 219–231. <https://doi.org/10.2138/am-2004-0126>
- Negro, F., Bousquet, R., Vils, F., Pellet, C.-M., & Hänggi-Schaub, J. (2013). Thermal structure and metamorphic evolution of the Piemont-Ligurian metasediments in the northern Western Alps. *Swiss Journal of Geosciences*, *106*(1), 63–78. <https://doi.org/10.1007/s00015-013-0119-7>
- Nibourel, L., Berger, A., Egli, D., Heuberger, S., & Herwegh, M. (2021). Structural and thermal evolution of the eastern Aar Massif: Insights from structural field work and Raman thermometry. *Swiss Journal of Geosciences*, *114*(1), 1–43. <https://doi.org/10.1186/s00015-020-00381-3>
- Nibourel, L., Berger, A., Egli, D., Luensdorf, N. K., & Herwegh, M. (2018). Large vertical displacements of a crystalline massif recorded by Raman thermometry. *Geology*, *46*(10), 879–882. <https://doi.org/10.1130/G45121.1>

- Nocquet, J.-M., Sue, C., Walpersdorf, A., Tran, T., Lenôtre, N., Vernant, P., et al. (2016). Present-day uplift of the western Alps. *Scientific Reports*, 6, 28404. <https://doi.org/10.1038/srep28404>
- Persaud, M., & Pfiffner, O. A. (2004). Active deformation in the eastern Swiss Alps: Post-glacial faults, seismicity and surface uplift. *Tectonophysics*, 385(1–4), 59–84. <https://doi.org/10.1016/j.tecto.2004.04.020>
- Peters, M. (2012). *Spatial distribution of quartz recrystallization microstructures in the Aar massif (Swiss Central Alps)* (Master thesis, unpublished). Universität Bern.
- Pfiffner, O.-A. (1972). Neue Kenntnisse zur Geologie östlich und westlich des Kunkelspasses (GR). *Eclogae Geologicae Helveticae*, 65(3), 555–562. <https://doi.org/10.5169/seals-164105>
- Pfiffner, O.-A. (1978). Der Falten- und Kleindeckenbau im infrahelvetikum der Ostschweiz. *Eclogae Geologicae Helveticae*, 71(1), 61–84. <https://doi.org/10.5169/seals-164718>
- Pfiffner, O. A. (1990). Kinematics and intrabed-strain in mesoscopically folded limestone layers: Examples from the Jura and the Helvetic Zone of the Alps. *Eclogae Geologicae Helveticae*, 83(3), 585–602.
- Pfiffner, O. A. (2011). *Structural Map of the Helvetic Zone of the Swiss Alps, including Vorarlberg (Austria) and Haute Savoie (France)*, 1:100 000. Geological Special Map, swisstopo, Explanatory notes 128.
- Pfiffner, O. A. (2015). *Geologie der Alpen* (3rd ed.). Haupt.
- Pfiffner, O. A., Lehner, P., Heitzmann, P., Mueller, S., & Steck, A. (1997). *Deep structure of the Swiss Alps: Results of NRP 20*. Birkhäuser.
- Price, J. B., Wernicke, B. P., Cosca, M. A., & Farley, K. A. (2018). Thermochronometry across the Austroalpine-Pennine boundary, Central Alps, Switzerland: Orogen-perpendicular normal fault slip on a major “overthrust” and its implications for orogenesis. *Tectonics*, 37, 1–34. <https://doi.org/10.1002/2017TC004619>
- Rahn, M. (1994). *Incipient metamorphism of the Glarus Alps: Petrology of the Taveyanne Greywacke and fission track dating* (PhD thesis, unpublished). Universität Basel.
- Rahn, M. (2001). *The metamorphic and exhumation history of the Helvetic Alps, Switzerland, as revealed by apatite and zircon fission tracks* (Habilitation thesis, unpublished). Albert Ludwigs Universität Freiburg.
- Rahn, M., Brandon, M. T., Batt, G. E., & Garver, J. I. (2004). A zero-damage model for fission-track annealing in zircon. *American Mineralogist*, 89(4), 473–484. <https://doi.org/10.2138/am-2004-0401>
- Rahn, M., & Grasemann, B. (1999). Fission track and numerical thermal modeling of differential exhumation of the Glarus thrust plane (Switzerland). *Earth and Planetary Science Letters*, 169(3–4), 245–259. [https://doi.org/10.1016/S0012-821X\(99\)00078-3](https://doi.org/10.1016/S0012-821X(99)00078-3)
- Rahn, M., Hurford, A., & Frey, M. (1997). Rotation and exhumation of a thrust plane: Apatite fission-track data from the Glarus thrust, Switzerland. *Geology*, 25(7), 599–602. [https://doi.org/10.1130/0091-7613\(1997\)025<0599:raeoat>2.3.co;2](https://doi.org/10.1130/0091-7613(1997)025<0599:raeoat>2.3.co;2)
- Ramsay, J. G., Casey, M., & Kligfield, R. (1983). Role of shear in development of the Helvetic fold-thrust belt of Switzerland. *Geology*, 11(8), 439–442. [https://doi.org/10.1130/0091-7613\(1983\)11<439:rosido>2.0.co;2](https://doi.org/10.1130/0091-7613(1983)11<439:rosido>2.0.co;2)
- Reinecker, J., Danišik, M., Schmid, C., Glotzbach, C., Rahn, M. K., Frisch, W., & Spiegel, C. (2008). Tectonic control on the late stage exhumation of the Aar Massif (Switzerland): Constraints from apatite fission track and (U-Th)/He data. *Tectonics*, 27(6), TC6009. <https://doi.org/10.1029/2007TC002247>
- Reiners, P. W., & Brandon, M. T. (2006). Using thermochronology to understand orogenic erosion. *Annual Review of Earth and Planetary Sciences*, 34(1), 419–466. <https://doi.org/10.1146/annurev.earth.34.031405.125202>
- Reiners, P. W., Farley, K. A., & Hickey, H. J. (2002). He diffusion and (U-Th)/He thermochronometry of zircon: Initial results from Fish Canyon Tuff and Gold Butte. *Tectonophysics*, 349(1–4), 297–308. [https://doi.org/10.1016/S0040-1951\(02\)00058-6](https://doi.org/10.1016/S0040-1951(02)00058-6)
- Ricchi, E., Bergemann, C., Gnos, E., Berger, A., Rubatto, D., & Whitehouse, M. (2019). Constraining deformation phases in the Aar Massif and the Gotthard Nappe (Switzerland) using Th-Pb crystallization ages of fissure monazite-(Ce). *Lithos*, 342, 223–238. <https://doi.org/10.1016/j.lithos.2019.04.014>
- Robert, X., van der Beek, P., Braun, J., Perry, C., & Mugnier, J.-L. (2011). Control of detachment geometry on lateral variations in exhumation rates in the Himalaya: Insights from low-temperature thermochronology and numerical modeling. *Journal of Geophysical Research*, 116(B5). <https://doi.org/10.1029/2010JB007893>
- Rolland, Y., Cox, S. F., & Corsini, M. (2009). Constraining deformation stages in brittle–ductile shear zones from combined field mapping and 40Ar/39Ar dating: The structural evolution of the Grimsel Pass area (Aar Massif, Swiss Alps). *Journal of Structural Geology*, 31(11), 1377–1394. <https://doi.org/10.1016/j.jsg.2009.08.003>
- Rosenberg, C. L., Schneider, S., Scharf, A., Bertrand, A., Hammerschmidt, K., Rabaute, A., & Brun, J.-P. (2018). Relating collisional kinematics to exhumation processes in the Eastern Alps. *Earth-Science Reviews*, 176, 311–344. <https://doi.org/10.1016/j.earscirev.2017.10.013>
- Schaer, J.-P., Reimer, G., & Wagner, G. (1975). Actual and ancient uplift rate in the Gotthard region, Swiss Alps: A comparison between precise levelling and fission-track apatite age. In *Developments in geotectonics* (Vol. 9, pp. 293–300). Elsevier. <https://doi.org/10.1016/B978-0-444-41420-5.50035-6>
- Schlatter, A. (2014). *Kinematische Gesamtausgleichung der Schweizer Landesnivellamentlinien 2013 und Detaildarstellung der rezenten vertikalen Oberflächenbewegungen in der Zentralschweiz* (pp. 14–38). Nagra Arbeitsbericht, NAB.
- Schlunegger, F., & Hinderer, M. (2001). Crustal uplift in the Alps: Why the drainage pattern matters. *Terra Nova*, 13(6), 425–432. <https://doi.org/10.1046/j.1365-3121.2001.00374.x>
- Schlunegger, F., & Kissling, E. (2015). Slab rollback orogeny in the Alps and evolution of the Swiss Molasse basin. *Nature Communications*, 6, 8605. <https://doi.org/10.1038/ncomms9605>
- Schlunegger, F., Matter, A., Burbank, D. W., & Klaper, E. M. (1997). Magnetostratigraphic constraints on relationships between evolution of the central Swiss Molasse basin and Alpine orogenic events. *Geological Society of America Bulletin*, 109(2), 225–241. [https://doi.org/10.1130/0016-7606\(1997\)109<0225:mcorbe>2.3.co;2](https://doi.org/10.1130/0016-7606(1997)109<0225:mcorbe>2.3.co;2)
- Schlunegger, F., & Mosar, J. (2011). The last erosional stage of the Molasse Basin and the Alps. *International Journal of Earth Sciences*, 100(5), 1147–1162. <https://doi.org/10.1007/s00531-010-0607-1>
- Schmid, S. M. (1975). The Glarus overthrust: Field evidence and mechanical model. *Eclogae Geologicae Helveticae*, 68, 247–280. <https://doi.org/10.5169/seals-164386>
- Schmid, S. M., Fügenschuh, B., Kissling, E., & Schuster, R. (2004). Tectonic map and overall architecture of the Alpine orogen. *Eclogae Geologicae Helveticae*, 97(1), 93–117. <https://doi.org/10.1007/s00015-004-1113-x>
- Schmid, S. M., Pfiffner, O. A., Froitzheim, N., Schönborn, G., & Kissling, E. (1996). Geophysical-geological transect and tectonic evolution of the Swiss-Italian Alps. *Tectonics*, 15(5), 1036–1064. <https://doi.org/10.1029/96TC00433>
- Schwartz, S., Gautheron, C., Audin, L., Dumont, T., Nomade, J., Barbarand, J., et al. (2017). Foreland exhumation controlled by crustal thickening in the Western Alps. *Geology*, 45(2), 139–142. <https://doi.org/10.1130/G38561.1>

- Seguinot, J., Ivy-Ochs, S., Jouvét, G., Huss, M., Funk, M., & Preusser, F. (2018). Modelling last glacial cycle ice dynamics in the Alps. *The Cryosphere*, 12(10), 3265–3285. <https://doi.org/10.5194/tc-12-3265-2018>
- Shi, Y., & Wang, C.-Y. (1987). Two-dimensional modeling of the p-t-t paths of regional metamorphism in simple overthrust terrains. *Geology*, 15(11), 1048–1051. [https://doi.org/10.1130/0091-7613\(1987\)15<1048:tmotpp>2.0.co;2](https://doi.org/10.1130/0091-7613(1987)15<1048:tmotpp>2.0.co;2)
- Simoes, M., Avouac, J. P., Beysac, O., Goffé, B., Farley, K. A., & Chen, Y.-G. (2007). Mountain building in Taiwan: A thermokinematic model. *Journal of Geophysical Research*, 112(B11). <https://doi.org/10.1029/2006JB004824>
- Spiegel, C., Kuhlemann, J., Dunkl, I., & Frisch, W. (2001). Paleogeography and catchment evolution in a mobile orogenic belt: The Central Alps in Oligo–Miocene times. *Tectonophysics*, 341(1–4), 33–47. [https://doi.org/10.1016/S0040-1951\(01\)00187-1](https://doi.org/10.1016/S0040-1951(01)00187-1)
- Spiegel, C., Kuhlemann, J., Dunkl, I., Frisch, W., von Eynatten, H., & Balogh, K. (2000). The erosion history of the Central Alps: Evidence from zircon fission track data of the foreland basin sediments. *Terra Nova*, 12(4), 163–170. <https://doi.org/10.1046/j.1365-3121.2000.00289.x>
- Stalder, N. F., Herman, F., Fellin, G. M., Coutand, I., Aguilar, G., Reiners, P. W., & Fox, M. (2020). The relationships between tectonics, climate and exhumation in the Central Andes (18–36 s): Evidence from low-temperature thermochronology. *Earth-Science Reviews*, 210, 103276. <https://doi.org/10.1016/j.earscirev.2020.103276>
- Steck, A. (1968). Die alpidischen Strukturen in den Zentralen Aaregraniten des westlichen Aarmassivs. *Eclogae Geologicae Helvetiae*, 61, 19–48. <https://doi.org/10.5169/seals-163584>
- Steiner, H. (1984). Mineralogisch-petrographische, geochemische und isotopengeologische Untersuchungen an einem Meta-Lamprophyrt und seinem granodioritischen Nebengestein (Matorello-Gneis) aus der Maggia-Decke. *Schweizerische Mineralogische und Petrographische Mitteilungen*, 64(1–2), 261–271. <https://doi.org/10.5169/seals-49544>
- Sternai, P., Sue, C., Husson, L., Serpelloni, E., Becker, T. W., Willett, S. D., et al. (2019). Present-day uplift of the European Alps: Evaluating mechanisms and models of their relative contributions. *Earth-Science Reviews*, 190, 589–604. <https://doi.org/10.1016/j.earscirev.2019.01.005>
- Stockli, D. F. (2005). Application of low-temperature thermochronometry to extensional tectonic settings. *Reviews in Mineralogy and Geochemistry*, 58(1), 411–448. <https://doi.org/10.2138/rmg.2005.58.16>
- Stüwe, K., White, L., & Brown, R. (1994). The influence of eroding topography on steady-state isotherms. Application to fission track analysis. *Earth and Planetary Science Letters*, 124(1–4), 63–74. [https://doi.org/10.1016/0012-821X\(94\)00068-9](https://doi.org/10.1016/0012-821X(94)00068-9)
- Sue, C., Delacou, B., Champagnac, J.-D., Allanic, C., Tricart, P., & Burkhard, M. (2007). Extensional neotectonics around the bend of the Western/Central Alps: An overview. *International Journal of Earth Sciences*, 96(6), 1101–1129. <https://doi.org/10.1007/s00531-007-0181-3>
- Tagami, T., Galbraith, R., Yamada, R., & Laslett, G. (1998). Revised annealing kinetics of fission tracks in zircon and geological implications. In *Advances in fission-track geochronology* (pp. 99–112). Springer. https://doi.org/10.1007/978-94-015-9133-1_8
- Tarantola, A. (2005). *Inverse problem theory and methods for model parameter estimation*. Siam.
- Timar-Geng, Z., Grujic, D., & Rahn, M. (2004). Deformation at the Leventina-Simano nappe boundary, Central Alps, Switzerland. *Eclogae Geologicae Helvetiae*, 97(2), 265–278. <https://doi.org/10.1007/s00015-004-1121-4>
- Trümpy, R., Aubert, D., & Bernoulli, D. (1980). Geology of Switzerland: Geological excursions (Vol. 10). Wepf.
- Valla, P. G., Rahn, M., Shuster, D. L., & van der Beek, P. A. (2016). Multi-phase late-Neogene exhumation history of the Aar massif, Swiss central Alps. *Terra Nova*, 28(6), 383–393. <https://doi.org/10.1111/ter.12231>
- Valla, P. G., van der Beek, P. A., Shuster, D. L., Braun, J., Herman, F., Tassan-Got, L., & Gautheron, C. (2012). Late Neogene exhumation and relief development of the Aar and Aiguilles Rouges massifs (Swiss Alps) from low-temperature thermochronology modeling and $^4\text{He}/^3\text{He}$ thermochronometry. *Journal of Geophysical Research*, 117, F01004. <https://doi.org/10.1029/2011JF002043>
- van der Beek, P. A., Valla, P. G., Herman, F., Braun, J., Persano, C., Dobson, K. J., & Labrin, E. (2010). Inversion of thermochronological age–elevation profiles to extract independent estimates of denudation and relief history—II: Application to the French Western Alps. *Earth and Planetary Science Letters*, 296(1–2), 9–22. <https://doi.org/10.1016/j.epsl.2010.04.032>
- Vernon, A. J., van der Beek, P. A., & Sinclair, H. D. (2009). Spatial correlation between long-term exhumation rates and present-day forcing parameters in the western European Alps. *Geology*, 37(9), 859–862. <https://doi.org/10.1130/G25740A.1>
- Vernon, A. J., van der Beek, P. A., Sinclair, H. D., Persano, C., Foeken, J., & Stuart, F. M. (2009). Variable late Neogene exhumation of the central European Alps: Low-temperature thermochronology from the Aar Massif, Switzerland, and the Lepontine Dome, Italy. *Tectonics*, 28(5), TC5004. <https://doi.org/10.1029/2008TC002387>
- Vernon, A. J., van der Beek, P. A., Sinclair, H. D., & Rahn, M. K. (2008). Increase in late Neogene denudation of the European Alps confirmed by analysis of a fission-track thermochronology database. *Earth and Planetary Science Letters*, 270(3–4), 316–329. <https://doi.org/10.1016/j.epsl.2008.03.053>
- von Däniken, P. A., & Frehner, M. (2017). 3D structural model and kinematic interpretation of the Panixer Pass Transverse Zone (Infralhelvetic Complex, eastern Switzerland). *Swiss Journal of Geosciences*, 110(2), 653–675. <https://doi.org/10.1007/s00015-016-0230-7>
- von Hagke, C., Cederbom, C. E., Oncken, O., Stöckli, D. F., Rahn, M. K., & Schlunegger, F. (2012). Linking the northern Alps with their foreland: The latest exhumation history resolved by low-temperature thermochronology. *Tectonics*, 31(5), TC5010. <https://doi.org/10.1029/2011TC003078>
- von Hagke, C., Oncken, O., Ortner, H., Cederbom, C. E., & Aichholzer, S. (2014). Late Miocene to present deformation and erosion of the Central Alps—Evidence for steady state mountain building from thermokinematic data. *Tectonophysics*, 632, 250–260. <https://doi.org/10.1016/j.tecto.2014.06.021>
- Wagner, G., Miller, D. S., & Jäger, E. (1979). Fission track ages on apatite of Bergell rocks from central Alps and Bergell boulders in Oligocene sediments. *Earth and Planetary Science Letters*, 45(2), 355–360. [https://doi.org/10.1016/0012-821X\(79\)90136-5](https://doi.org/10.1016/0012-821X(79)90136-5)
- Wagner, G., & Reimer, G. (1972). Fission track tectonics: The tectonic interpretation of fission track apatite ages. *Earth and Planetary Science Letters*, 14(2), 263–268. [https://doi.org/10.1016/0012-821X\(72\)90018-0](https://doi.org/10.1016/0012-821X(72)90018-0)
- Wagner, G., Reimer, G., & Jäger, E. (1977). *Cooling ages derived by apatite fission-track, mica Rb-Sr and K-Ar dating: the uplift and cooling history of the Central Alps* (Vol. 30, pp. 1–27). Memoirs of the Institute of Geology and Mineralogy, University of Padova.
- Wangenheim, C. (2016). *Quantifying fluvial and glacial erosion using (detrital) thermochronology, cosmogenic nuclides and numerical modelling: A case study in the European Alps* (PhD thesis, unpublished). Gottfried Wilhelm Leibniz Universität Hannover.
- Weh, M. (1998). *Tektonische entwicklung der penninischen sediment-decken in graubünden (präätigau bis oberhalbstein)* (PhD thesis, unpublished). Universität Basel.
- Wehrens, P., Baumberger, R., Berger, A., & Herwegh, M. (2017). How is strain localized in a meta-granitoid, mid-crustal basement section? Spatial distribution of deformation in the central Aar massif (Switzerland). *Journal of Structural Geology*, 94, 47–67. <https://doi.org/10.1016/j.jsg.2016.11.004>

- Weisenberger, T. B., Rahn, M. K., van der Lelij, R., Spikings, R. A., & Bucher, K. (2012). Timing of low-temperature mineral formation during exhumation and cooling in the Central Alps, Switzerland. *Earth and Planetary Science Letters*, 327–328, 1–8. <https://doi.org/10.1016/j.epsl.2012.01.007>
- Wiederkehr, M., Bousquet, R., Ziemann, M. A., Berger, A., & Schmid, S. M. (2011). 3-d assessment of peak-metamorphic conditions by Raman spectroscopy of carbonaceous material: An example from the margin of the lepontine dome (Swiss Central Alps). *International Journal of Earth Sciences*, 100(5), 1029–1063. <https://doi.org/10.1007/s00531-010-0622-2>
- Willett, S. D. (2010). Late Neogene erosion of the Alps: A climate driver? *Annual Review of Earth and Planetary Sciences*, 38(1), 411–437. <https://doi.org/10.1146/annurev-earth-040809-152543>
- Willett, S. D., & Brandon, M. T. (2013). Some analytical methods for converting thermochronometric age to erosion rate. *Geochemistry, Geophysics, Geosystems*, 14(1), 209–222. <https://doi.org/10.1029/2012GC004279>
- Willett, S. D., Herman, F., Fox, M., Stalder, N., Ehlers, T. A., Jiao, R., & Yang, R. (2020). Bias and error in modelling thermochronometric data: Resolving a potential increase in plio-pleistocene erosion rate. *Earth Surface Dynamics Discussions*, 9, 1–78. <https://doi.org/10.5194/esurf-2020-59>
- Willett, S. D., Schlunegger, F., & Picotti, V. (2006). Messinian climate change and erosional destruction of the central European Alps. *Geology*, 34(8), 613. <https://doi.org/10.1130/G22280.1>
- Wittmann, H., von Blanckenburg, F., Kruesmann, T., Norton, K. P., & Kubik, P. W. (2007). Relation between rock uplift and denudation from cosmogenic nuclides in river sediment in the Central Alps of Switzerland. *Journal of Geophysical Research*, 112(F4). <https://doi.org/10.1029/2006JF000729>
- Zachos, J., Pagani, M., Sloan, L., Thomas, E., & Billups, K. (2001). Trends, rhythms, and aberrations in global climate 65 Ma to present. *Science*, 292(5517), 686–693. <https://doi.org/10.1126/science.1059412>
- Zerlauth, M., Ortner, H., Pomella, H., Adrian Pfiffner, O., & Fügenschuh, B. (2014). Inherited tectonic structures controlling the deformation style: An example from the Helvetic nappes of the Eastern Alps. *Swiss Journal of Geosciences*, 107(2–3), 157–175. <https://doi.org/10.1007/s00015-014-0167-7>